# Structured Overset and Unstructured Grid Simulations for the Third AIAA Sonic Boom Prediction Workshop

Jared C. Duensing*, James C. Jensen†, Jeffrey A. Housman‡, Michael G. Piotrowski§, Gaetan K. Kenway¶, Daniel Maldonado‖, Emre Sozer**, and Cetin C. Kiris††

*NASA Ames Research Center, M/S 258-2, Moffett Field, CA 94035*

**Predictions using the Launch Ascent and Vehicle Aerodynamics (LAVA) Unstructured and Structured Curvilinear solvers for the Biconvex and C608 geometries are compared in support of the 3rd AIAA Sonic Boom Prediction workshop. Description of the mesh generation techniques and numerical methods are provided along with a comparison of nearfield and far-field predictions with available experimental data as well as other workshop submissions. Strong consistency was observed between the Biconvex and C608 nearfield predictions across the two solvers used for this study, as well as validation and verification data. Additionally, near-field and farfield ground signature results using a combination of a truncated computational fluid dynamics (CFD) domain coupled to a mid-field space marching method and propagated to the ground using sBOOM will be discussed. This approach is shown to provide an efficient way to propagate near-field pressure signatures to the ground with the same accuracy as the near-field CFD coupled to sBOOM, but at less computational cost.**

## I. Nomenclature

| | | |
|---|---|---|
| $CFL$ | = | Courant-Friedrichs-Lewy number |
| $L_{body}$ | = | model body length |
| $M$ | = | Mach number |
| $NPR$ | = | nozzle pressure ratio |
| $P_{static}/P_{static,fs}$ | = | static to freestream pressure ratio |
| $P_{total}/P_{static,fs}$ | = | total to freestream pressure ratio |
| $R$ | = | radial distance from model centerline |
| $T_{total}/T_{static,fs}$ | = | total to freestream temperature ratio |
| $X$ | = | position relative to nose in the freestream direction |
| $\alpha$ | = | aircraft angle of attack |
| $\mu$ | = | Mach cone angle |
| $\Delta p/P_\infty$ | = | pressure disturbance normalized by freestream pressure |
| $\phi$ | = | off-track angle |

* *Computational Aerosciences Branch, AIAA Member, jared.c.duensing@nasa.gov*
† *Computational Aerosciences Branch, AIAA Member, james.c.jensen@nasa.gov*
‡ *Computational Aerosciences Branch, AIAA Senior Member, jeffrey.a.housman@nasa.gov*
§ *Computational Aerosciences Branch, AIAA Member, jeffrey.a.housman@nasa.gov*
¶ *Science and Technology Corporation, AIAA Member, gaetan.k.kenway@nasa.gov*
‖ *Computational Aerosciences Branch, AIAA Member, daniel.maldonado@nasa.gov*
** *Computational Aerosciences Branch, AIAA Member, emre.sozer@nasa.gov*
†† *Computational Aerosciences Branch, AIAA Senior Member, cetin.c.kiris@nasa.gov*

## II. Introduction

In recent years, NASA in collaboration with the aerospace industry has performed extensive research committed to making supersonic commercial flight a reality. One of the greatest challenges facing engineers and scientists in this field is the development of an aircraft design that minimizes the ground-noise characteristics of supersonic flight. A key component of this design process is the use of high-fidelity computational fluid dynamics (CFD) to predict the noise levels generated by a given aircraft design, and evaluate the sources of noise generation to influence the design process. Through the Third Sonic Boom Prediction Workshop (SBPW3) hosted by the American Institute of Aeronautics and Astronautics (AIAA), workshop participants utilized a variety of CFD solvers to make noise predictions for two supersonic test cases. The ensemble of solution data provided to the workshop, alongside experimental data provided by the committee, served as the verification and validation required to ensure CFD predictions are accurate. The Launch Ascent and Vehicle Aerodynamics (LAVA)[1] team participated in the SBPW3 workshop, which was held on January 4-5th, 2020 at Orlando, Florida. The work presented at this conference directly follows the analysis presented during the First (SBPW1) and Second (SBPW2) workshops. In previous workshops, data was submitted for only the near-field portion of the workshop,[2,3] while additional analysis was performed for this workshop to examine the propagated noise levels on the ground and results for both the nearfield and propagated results will be discussed at length.

The nearfield portion of the workshop quantified pressure disturbance signatures, $\Delta p/P_\infty$, for two supersonic applications, the biconvex shock-plume interaction test article and the full-scale C608 quiet supersonic aircraft. The biconvex geometry was a wind tunnel model tested in the NASA Ames 9x7 ft. Supersonic Tunnel[4,5] and the C608 prototype was a design iteration from NASA's X-59 program. The workshop specified that a grid refinement study must be performed for both cases to study the sensitivity of acoustic predictions to mesh resolution. Required grid refinement study cases were completed for both geometries using the unstructured polyhedral and structured curvilinear solvers within the LAVA framework in order to verify that both solvers would yield consistent near-field predictions. In addition, the near-field signatures are propagated to the ground using the far-field sonic boom propagation code sBOOM[6] to compare the predicted loudness from the codes.

The workshop was also utilized to confirm that the best-practices established in previous workshops for both solvers still persisted for the latest versions of the LAVA code. One of the major developments within LAVA since SBPW2 was the refactoring of the curvilinear solver, which revised solver algorithms to be better suited for modern high-performance computing architectures. As a result of this code refactoring, computations in the supersonic flow regime could now be performed with up to a factor of 10 savings in computational resources. The CFD simulations performed during this workshop provided an opportunity to not only validate solution accuracy against experimental data, but also to verify the solutions obtained from the refactored version of LAVA Curvilinear and the LAVA Unstructured solver against other solver predictions.

The workshop also presented an opportunity to investigate utilization of the space marching solver[7] within LAVA in a three-step ground level noise prediction procedure. First, the near-field is predicted on a truncated CFD domain with a radial extent that is a factor of 8 smaller than the workshop grid. Next, the high-order accurate space marching method is used to efficiently propagate the near-field solution to the mid-field. Finally, the solution is coupled to sBOOM for ground level noise prediction. In addition to the workshop specified coupling location of three body lengths, coupling locations of six and nine body lengths are also presented showing the benefit of the space marching method to assess the sensitivity to sBOOM coupling location.

## III. Computational Methodology

The LAVA solver framework provides the capability to use multiple mesh paradigms to simulate complex geometries for a wide variety of aerospace applications.[1] The LAVA Curvilinear and Unstructured solvers are utilized for all workshop analysis, which supports structured curvilinear and unstructured arbitrary polyhedral meshes, respectively. A variety of numerical schemes for spatial discretization are provided within the framework to solve the compressible Navier-Stokes equations. All workshop cases presented here are simulated using a steady-state Reynolds-Averaged Navier-Stokes (RANS) analysis approach using a fully-turbulent flow assumption. A second-order accurate modified Roe scheme and fourth-order accurate hybrid-

weighted compact nonlinear scheme (HWCNS)[8] are the convective flux discretizations for all structured curvilinear workshop simulations, while the unstructured simulations utilize a second-order AUSMPW+[9] convective flux discretization. Both solvers also contain multiple turbulence models for RANS closure, including the Spalart-Allmaras (SA)[10] and Shear Stress Transport (SST)[11] models. The structured and unstructured workshop simulations both use the SA turbulence model, while the structured curvilinear simulations use the rotation correction (RC)[12] and quadratic constitutive relation (QCR2000).[13] Finally, various flux limiter options available within both solvers were utilized to limit solution gradients in the supersonic regime. A summary of solver options used for the workshop problems are provided in Table 1. For the C608 supersonic aircraft case, the HWCNS scheme was not utilized for LAVA Curvilinear simulations.

The recent refactoring of the curvilinear solver has prompted the repeat of workshop simulations to verify predictions between both versions of the solver are consistent. All numerical schemes and settings were consistent between the production and refactored curvilinear simulations, however the production version uses an Alternating line-Jacobi relaxation linear solver while the refactored version uses the ILU preconditioned generalized minimal residual method (GMRES) linear solver.[14] This update has demonstrated deeper steady-state solution convergence as compared to the production solver solutions, results of which will be discussed at length.

**Table 1. Numerical Selections for Workshop CFD Simulations**

| Mesh Paradigm | Convective Flux | Linear Solver | Flux Limiter | Turbulence Model |
|---|---|---|---|---|
| Structured Curvilinear | Modified Roe | GMRES | Koren | SA-RC-QCR2000 |
| Structured Curvilinear | HWCNS | GMRES | WENO | SA-RC-QCR2000 |
| Unstructured Polyhedral | AUSMPW+ | GMRES | minmod | SA |

In addition to using the LAVA CFD solvers for near-field prediction, the LAVA Space Marching solver was used for mid-field predictions and both approaches were propagated to the ground using the sBOOM far-field sonic boom propagation code. sBOOM was developed by Sriram Rallabhandi at NASA Langley to propagate pressure signals through the atmosphere using an augmented Burgers equation. The code has the option to use specified atmospheric temperature and wind profiles, but for this work the propagations were performed assuming standard atmospheric conditions without any wind.

# IV. Results

## IV.A. Biconvex 9x7 Shock-Plume Interaction Model

The first model analyzed for the SBPW3 is known as the biconvex shock generator of the shock-plume interaction model tested in the NASA Ames 9- by 7-ft Supersonic Wind Tunnel in February of 2016. Model geometry consists of a nozzle with a conical nose facing the oncoming flow and internal ducting through which high-pressure air is pumped to produce the jet exhausted through the aft end of the model. Additionally, the sting mounting hardware is included in the simulation along with the wing-like biconvex geometry, designed to mimic the shock interaction effects of a conventional T-tail with the engine exhaust plume. Figure 1 provides multiple perspectives of the CAD geometry used for CFD simulation. Experimental data was collected at a freestream Mach of 1.6 and 2.0 at varying nozzle pressure ratios (NPR), $P_{total}/P_{static,fs}$, however the workshop simulations focus on the Mach 1.6, NPR = 8.0 condition. Other condition specifications include an angle of attack, $\alpha$, of 0.0°, freestream temperature of $374°R$, a Reynolds number based on freestream of $376,850in^{-1}$, and an engine total temperature ratio, $T_{total}/T_{static,fs}$, of 1.768. A subsonic inflow boundary condition is applied to the nozzle inlet face, which extrapolates Mach number and utilizes the stagnation pressure and temperature computed from the given total ratios to prescribe all states based on isentropic flow relations. Because experimental data for this workshop subtask was provided by the committee, the biconvex nearfield CFD analysis served as a critical validation step for all workshop CFD efforts. Pressure disturbance data, $\Delta p/P_\infty$, would be extracted from the CFD solutions at 3.0 body lengths from the model, at azimuthal locations, $\phi$, of 0.0°, 15.0°, and 30.0° consistent with experimental data collected.

## IV.B. Computational Mesh Generation

The authors of this work elected to generate original computational grids from the CAD representation of the model, which was provided by the workshop in Initial Graphics Exchange Specification (IGES) format.

Generating these meshes enabled the LAVA team to perform the analysis using two unique solvers within the framework, providing assurance that CFD predictions are consistent using both mesh paradigms and codes.

### *IV.B.1. Structured Overset Grids*

For the structured curvilinear mesh generation, standard procedures were followed to discretize the surface geometry from the given CAD. The quality of the CAD provided by the committee did not require any modifications to surface quality, with the exception of fine features below a given tolerance slightly modified to allow structured overset mesh construction. These modifications were performed using the ANSA[15] software package. A new IGES formatted file was then exported to serve as the database for all mesh construction, which is performed using the Pointwise[16] software. Guidelines for mesh properties were established before the initial coarse mesh refinement level would be generated, which were based on overset grid systems generated for SBPW2.[17] These guidelines included a specification for leading edge spacings on wing-like features, set at 0.1% of the local chord length, maximum component spacing, set at 3% of the device characteristic length, number of points on all trailing edges, set to 5 points, and maximum stretching ratio, set at 1.2 for the initial grid. A minimum 5 point overlap between adjacent surface domains was also constructed to ensure adequate communication between fringe points of adjacent domains. A final elliptic smoothing and projection step onto the CAD geometry definition was performed to maximize the interior quality of each surface domain and ensure all points are constrained to the original geometry.

The final steps of the mesh generation procedure are performed in Chimera Grid Tools (CGT).[18] The plot3D (P3D) formatted surface domains exported from Pointwise are then hyperbolically extruded using CGT to construct the final body-fitted, boundary layer-resolving meshes. The initial cell height for all wall boundaries, $ds_{wall}$, was approximated such that the maximum wall spacing in viscous units was $y^+ \approx 1.0$ approximated from the freestream condition and flat plate boundary layer theory. Designing the off-body computational mesh to optimally capture supersonic flow features and gradients was also given a high level of scrutiny, and best-practices highlighted in Park *et. al.*[19] were applied. Supersonic aerodynamic theory defines the Mach angle as a inverse trigonometric function of Mach number, however numerical schemes used to discretize the convective flux terms are known to skew the Mach cone angle by a small value, $\mu_\epsilon$. This correction is therefore applied to better predict the Mach angle induced by the biconvex geometry and incorporating this discretization error, where $\mu_\epsilon = 0.2^\circ$ was selected based on previous research conducted by Housman *et. al.* for similar applications,[7]

$$\mu = sin^{-1}(1/M) + \mu_\epsilon \tag{1}$$

Therefore, the farfield mesh topology is designed by extruding a surface from the geometric centerline linearly in the direction of the Mach cone angle, and revolving the resulting surface about the geometric centerline. Special consideration of point redistribution in the axial, radial, and azimuthal directions was also necessary to ensure adequate spatial resolution was given to key features, particularly around regions of high-gradient. The axial distribution was initially designed based on geometrical features believed to be shock-inducing, such as the nozzle tip, sting, and biconvex. However, this distribution was further iterated upon based on initial CFD results obtained with both solvers, resulting in local coarsening and refining based on solution observations. The radial distribution was similarly determined based on required resolution around geometric features and commensurate spacing with adjacent body-fitted volume meshes, which also drove a similar redistribution in the azimuthal direction. The final farfield domain extended 3.0 nozzle body lengths radially outward from the geometry, and about 1.0 body lengths axially forward and aft of the model. Resolution of the mesh in the plume region was also adjusted by adding a refinement region to ensure that the structures produced by the nozzle jet could be well-resolved. The resulting mesh was then consistently refined by refinement ratios of 1.4 and 2.0 to produce the medium and fine level resolutions, which scales the number of points in all three curvilinear coordinate directions, globally reducing stretching ratios and mesh spacings. Figure 2 illustrates the final computational mesh and Table 2 summarizes final mesh statistics for all refinement levels.

Domain connectivity was the final step in the overset mesh generation process, which identifies valid donors for fringe points in overlapping regions and eliminates solve points from within physical boundaries. This two-step process first uses the OVERFLOW[20] connectivity routine to minimally retract mesh points based on user-specified 'cutting' instructions. The second step is a pre-processing routine in the LAVA

curvilinear solver that optimizes the overset regions, in which points are kept as partial differential equation (PDE) solve points based on a cell volume heuristic, while a donor search algorithm is performed for any fringe points. One key update in the latest version of the solver includes improvement to the optimized connectivity routine. As a result of parallelization of this routine and an improved donor search algorithm, domain connectivity run time for the biconvex fine mesh case was reduced from 4 hours for the fine mesh case to around 6 minutes. Similar improvements were also observed for the coarser level meshes.

#### *IV.B.2. Unstructured Grids*

The unstructured mesh generation procedure follows a similar process with respect to mesh preparation. Because no modifications or clean-up was required to improve surface quality, the IGES representation of the geometry provided by the workshop was directly imported into Star-CCM+[21] for unstructured mesh generation. An initial unstructured triangulation was constructed on the biconvex geometry with a specified maximum cell size, stretching ratio, and resolution near leading and trailing edges, consistent with the coarse mesh guidelines for the structured mesh. Prism layer cells with a first cell height consistent with the structured overset volume meshes were extruded normal to the surface for sufficient boundary layer resolution. The prismatic cell layer then gives way to arbitrary polyhedral cells, which extend outward from the geometry to a cylindrical core surface at a predetermined distance away from the wall boundaries. This distance is chosen such that the entirety of geometry is enclosed using the smallest radius cylinder possible. The Mach-aligned layers are extruded from the cylinder radially outward at the Mach cone angle, which is determined from the freestream Mach number. The Mach-aligned portion of the mesh is constructed using a utility available within the LAVA Unstructured solver. An additional refinement region placed in the nozzle plume wake was also included to sufficiently resolve fluid structures aft of the nozzle, with cell sizes consistent with the refinement region generated in the structured overset mesh. Figure 3 presents the final surface and volume mesh for the coarse level case, with these features emphasized. Table 2 summarizes the resulting mesh sizes that would be utilized for the remainder of the mesh refinement study.

**Table 2. Computational mesh statistics for the biconvex shock-plume interaction case.**

| Mesh | Total Nodes/Cells (M) | Total Degrees of Freedom (M) |
|---|---|---|
| Structured overset (coarse) | 37.477 | 30.317 |
| Structured overset (medium) | 101.204 | 82.031 |
| Structured overset (fine) | 298.716 | 241.012 |
| Unstructured polyhedral (very coarse) | 7.423 | – |
| Unstructured polyhedral (coarse) | 12.362 | – |
| Unstructured polyhedral (medium) | 26.972 | – |
| Unstructured polyhedral (fine) | 55.088 | – |

### IV.C. Nearfield Pressure Signature Results

For all nearfield pressure disturbance sampling and comparisons, signatures were extracted from all LAVA CFD solutions at radial location $R = 15.1in$, which is approximately 67% of the total nozzle length. Figure 4 provides a sample LAVA Curvilinear pressure signature shown at this radial location of interest, along with sample pressure disturbance contours on the model symmetry plane that are characteristic of all LAVA solutions.

Curvilinear mesh refinement results for the modified Roe and HWCNS results would eventually be compared to study solution dependence on spatial resolution, however preliminary CFD simulations to determine appropriate solver parameters were first executed. Using the lower-order Roe scheme, these studies demonstrated the importance of solver input specifications, particularly due to the multiple flow regimes involved in this application. The subsonic nature of the nozzle outflow was an especially crucial factor in approaching simulation set-up, despite the majority of the computational domain residing in the supersonic regime. Initialization of the flow field to a predetermined subsonic condition inside the nozzle, while the remainder of the flow field is initialized to the supersonic freestream condition ensured the RANS equations would successfully converge the solution onto the correct side of the sonic barrier. The pseudo-time step, or CFL number, was mainly limited by the supersonic nature of the problem, and a value of 2.0 was found to be

most suitable for cases run at a fixed CFL. These methods were then applied to the higher-order HWCNS simulations on all mesh levels.

Additional features recently added to the curvilinear solver provided further benefits which were tested with the modified Roe scheme, which include:

- Automatic CFL number ramping capability
- ILU preconditioned GMRES linear solver
- Solution initialization with an arbitrary boundary layer height, scaling the freestream velocity components linearly to zero near all viscous wall boundaries
- Utility to interpolate primitive variables from one CFD solution onto another computational mesh, where freestream states are prescribed at any nodes unable to find a valid donor

Simulation wall time on all mesh levels benefitted from the automatic CFL number ramping capability, where a starting flow and turbulent CFL number of 1.0 was ramped to a maximum CFL number of 150.0 to accelerate steady-state convergence after numerical transients are attenuated. Additionally, solution interpolation allowed the converged solution on the coarse mesh to serve as an initialized solution for the medium and fine mesh levels, providing additional computational speed-up. An example of steady-state convergence behavior for the fine mesh simulation is provided in Fig. 5, which compares the normalized $L_2$ norm of the flow equation residuals as a function of wall clock time for the original solver using alternating line-Jacobi relaxation and the refactored solver using GMRES. A deeper level of steady-state convergence and about a 10X reduction wall clock time is obtained with the GMRES linear solver for the modified Roe scheme. It is anticipated that similar benefits will be observed using the HWCNS, but these results will be studied at a later time. Table 3 compares the execution time and total CPUs required for all HWCNS and Roe scheme results obtained with the original and refactored versions of the LAVA Curvilinear solver. With the combined ability to initialize finer mesh level simulations from coarser mesh solutions and the ability of the refactored solver to obtain deeper steady-state convergence in fewer nonlinear iterations, a 3-10X reduction in resource usage was observed for the Roe scheme simulations using the refactored solver. Unstructured resource usage is also given for comparison, which is on par with the Roe and HWCNS curvilinear simulations before the refactorization.

**Table 3. Resource usage for each biconvex simulation in CPU-hours with SBUs (Standard Billing Units on the Pleiades and Electra supercomputers depending on node type used) provided in parentheses.**

| Solver (Scheme) | Very Coarse | Coarse | Medium | Fine |
|---|---|---|---|---|
| LAVA Curvilinear (HWCNS) | – | 800 (26.4) | 2,880 (95.0) | 12,000 (396.0) |
| LAVA Curvilinear (Roe) | – | 800 (26.4) | 1,440 (47.5) | 12,000 (396.0) |
| LAVA Curvilinear Refactored (Roe) | – | 194 (8.15) | 186 (7.39) | 1,260 (50.1) |
| LAVA Unstructured (AUSMPW+) | 840 (30.0) | 1,680 (60.0) | 3,248 (116.0) | 11,200 (369.6) |

The final submitted nearfield pressure signature results on all mesh levels using the modified Roe scheme are shown in Figure 6. General trends seen in the pressure signatures are consistent across all refinement levels, with minor discrepancies observed in the magnitudes of the overpressure and underpressure peaks. This appears true for both numerical schemes presented. As anticipated, the increase in mesh resolution creates the 'sharper' detail generally observed in these local maxima and minima due to lessened dissipation in the finer mesh levels. Both the HWCNS results shown in Fig. 7 and the modified Roe scheme results appear to capture consistent shock patterns, and the slight variation is mainly confined to the peak behavior at local extrema. This variation corresponds to the expansion after the nozzle nose ($X = 32in$), the shock emerging from the nozzle lip ($X = 42in$), and the shock produced by the biconvex wing ($X = 46in$). It is also believed that some discrepancies might also be attributed to numerical artifacts and the depth of steady-state convergence dictated by the linear solver selection, the spatial order of the numerical scheme, and the chosen flux limiter.

Simulations for the unstructured solver required similar methodologies to obtain a steady-state converged solution for the biconvex geometry. Pressure signatures for the mesh refinement study are given in Fig. 8. Signature profiles exhibit characteristics similar to the curvilinear mesh refinement results, where most differences are confined to local extrema for reasons similar to curvilinear predictions. High frequency noise

content is also noted in the expansion region just aft of the nozzle nose, which is not present in the curvilinear predictions. This phenomenon is attributed to the faceting of the surface representation of the nose. Since the surface is constructed using arbitary polygons the cells don't have a consistent orientation like is found in a structured grid. This can lead to local inconsistencies in the curvature which can show up as small fluctuations in the pressure signal.

A final comparison between the fine mesh results for all LAVA curvilinear and unstructured simulations is presented in Fig. 9, comparing with 9- by 7-ft wind tunnel data to serve as validation of the biconvex CFD study. Error bars in the experiment denote the standard deviation in the collected wind tunnel data, while the solid curve represents the time-averaged signal. The general behavior of the profiles follows the experimental measurements, particularly at lower azimuths nearer to the on-track position. Discrepancies between CFD and experiment are mostly localized to signature extrema caused by the nozzle lip shock and biconvex wing, where CFD tends to overpredict these shock magnitudes greater than the experimental standard deviation, particularly at off-track azimuths. Speculation by the committee has attributed these differences mostly to test-section shock reflection not modeled in the free-air simulations as well as possible drift in reference pressure and angle of attack during the experiment. Furthermore, the complex flow physics in the shock-plume interaction region may not be adequately modeled using a steady-state RANS approach, but instead may require a higher-fidelity modeling method such as hybrid RANS-LES or DDES.[22] Most workshop participant CFD predictions also had the tendency to overshoot the experimental data in these regions, as demonstrated by the ensemble mean of all pressure signature submissions. Figure 10 compares the ensemble mean and standard deviation of all workshop profiles to the LAVA Curvilinear and Unstructured results on the finest level meshes. LAVA predictions generally agree strongly with the averaged signature and are entirely within one standard deviation of the mean across the length of the signature. This includes regions of the profile near overpressure and underpressure peaks, despite the demonstrated sensitivity to CFD solver specifications.

Comparisons of the complete boom carpet shown for $R = 15.1in$ in Fig. 11 further demonstrate the strong code agreement between the LAVA solvers, with notable differences only beginning to appear around $\phi = 90.0°$ and higher due to differences in mesh resolution. Because off-track angle profiles were only studied up to $\phi = 30.0°$, only the lower half of the boom carpet is presented. Also encouraging is the level of agreement in the biconvex shock-plume interaction region, where the solution uncertainty is typically the highest due to the complex, unsteady flow physics.[23]

Impulse was the final quantity of interest computed for the workshop, which was used to quantify the net effect of the overpressure and underpressure waves produced in the aft region of the nozzle, defined as:

$$1/P_\infty \int_{x_1}^{x_2} \Delta P(x) dx \tag{2}$$

This quantity was computed at each off-track position for all numerical schemes simulated and compared to the ensemble mean of all workshop submissions. All solutions predict a minimum impulse magnitude at $\phi = 15°$, with similar magnitudes at $\phi = 0°$ and $\phi = 30°$. From a low-boom perspective, this demonstrates the importance of accurate CFD predictions at positions well off-track, as high-sound content of concern to low-boom applications such as the C608 is likely contained across the boom carpet. The modified Roe and AUSMPW+ predictions computed from the curvilinear and unstructured simulations were predicted to within 3.4% of the ensemble mean, while the higher-order HWCNS prediction computed from the curvilinear solution was within 11.5% of the mean across all azimuths. All biconvex impulse predictions were therefore within the standard deviation of workshop submissions, with the exception of the on-track HWCNS prediction. Figure 12 presents the calculated impulse for all numerical schemes and azimuths compared to the ensemble mean. Due to the difficulty in achieving a deeply converged steady-state solution with the HWCNS, it is possible that high-order numerics prevented the flow solver from achieving adequate steady-state convergence. Future work on this problem will involve simulating the HWCNS case using the ILU preconditioned GMRES linear solver to determine if steady-state convergence can be improved.

### IV.D. X-59 C608 Prototype Model

The X-59 C608 prototype design concept was the second workshop geometry assessed as part of the CFD predictions of nearfield acoustic behavior. The model consists of a highly swept wing with a half-span planform area of $400.0ft^2$, a total length of $90.0ft$, and a design angle of attack of $2.15°$. The flow condition is representative of high-altitude cruise flight, where standard atmosphere is assumed at $53,200ft$ and a

freestream temperature of $389.9°R$, Reynolds number of $109,776in^{-1}$, and freestream Mach number of 1.4 are used. Multiple intakes and exhaust ducts on the aircraft are also modeled, which are treated as inflow and outflow boundary conditions to the CFD computational domain. These are the engine fan face where $P_{static}/P_{static,fs} = 2.6$, the environmental control system (ECS) inlet face with $P_{static}/P_{static,fs} = 1.4$, the engine exhaust plenum chamber where $P_{total}/P_{static,fs} = 10.0$ and $T_{total}/T_{static,fs} = 7.0$, and the engine bypass exhaust with $P_{total}/P_{static,fs} = 2.4$ and $T_{total}/T_{static,fs} = 2.0$. Subsonic outflow boundary conditions which prescribe static pressure and extrapolate all other states would be applied to all air intake boundaries, while all engine exhaust boundaries are set by the stagnation pressure and temperature that prescribe all states through isentropic flow equations. Locations of all air intakes and outflows are provided in Fig. 13 with views of the model from multiple perspectives. Workshop participants were assigned to extract pressure signature data at multiple azimuthal locations, $\phi$, from $0.0°$ to $180.0°$ in increments of $2.0°$, and the ensemble average of this data would serve as verification for the LAVA Curvilinear and Unstructured predictions. These nearfield extractions were all taken at a radial distance of $R = 3L$, where $L$ is the total length of the aircraft. Additional quantities related to loudness were computed by the committee and will be briefly discussed, including the perceived level (PL) and A-weighted sound exposure level (ASEL) for each azimuth at this radial distance from the aircraft. All LAVA Curvilinear CFD results were produced using the recently refactored version of the solver discussed previously, however a summary of the computational savings will be given by comparing C608 cases run with the solver prior to the refactoring process. The same version of the LAVA Unstructured solver utilized for the biconvex analysis was used for the C608 analysis and any modifications to the solver input parameters will be discussed.

### IV.E. Computational Mesh Generation

The CAD representation of the C608 geometry was provided in IGES format and was used to generate original structured overset and unstructured arbitrary polyhedral grids using generic best-practices for low supersonic applications, previous workshop lessons learned, and takeaways from the biconvex workshop problem.

Structured curvilinear mesh generation procedures closely followed the steps outlined in Subsection IV.B for the biconvex case. The CAD required only minor modifications using the ANSA software, such as simplification of tight gaps and corners which prevent structured surface mesh generation. Special consideration was also given into how the surface would be decomposed into quadrilateral patches, boundaries of which would be used for individual surface mesh domains. The final database used for all surface mesh generation in Pointwise was defined by this modified IGES representation, and structured overlapping patches were generated within this software. Guidelines used for the coarse level surface mesh generation were consistent with guidelines established for the biconvex nozzle geometry, and the resulting structured meshes were exported as plot3D (P3D) formatted domains. The CGT software was then utilized to extrude the surface meshes hyperbolically to produce the final body-fitted domains. Based on the freestream flow condition and flat plate boundary layer theory, the initial cell height was selected for all wall boundaries such that maximum wall spacing in viscous units was $y^+ \approx 1.0$.

Special attention was once again applied to the off-body mesh design to ensure adequate resolution could capture key supersonic flow features, as outlined in Subsection IV.B. Once again, a Mach aligned conical mesh was generated and the extent of the farfield boundaries was consistent with the biconvex case, in which the domain extended 4.0 aircraft body lengths radially outward, 1.0 body lengths forward, and 2.0 body lengths aft of the geometry. Point redistribution in the axial, radial, and azimuthal directions was dictated by regions predicted to contain large gradients in the flow field, and this redistribution process was further iterated following preliminary computations. Due to the geometric complexity of the C608 relative to the biconvex, the axial redistribution of points was critical to ensure all shocks induced by geometric features and protuberances would be adequately resolved. Many shock-inducing features present from the nose to tail section warranted the need for relatively fine resolution across all axial locations, with the exception of the relatively benign region between the nose and canard. Utimately, a relatively fine, nearly uniform distribution was necessary to resolve all pressure disturbance features from the canard to the tail section, with an additional refinement region at the aircraft nose shown in Fig. 14. The radial and azimuthal distributions were selected to provide sufficient resolution near the body of the aircraft and were stretched to much larger cell sizes at the farfield boundaries. As was the case for the biconvex, the coarse level mesh distributions would be iterated upon following preliminary CFD simulations used to understand the flow field at hand. The resulting mesh would serve as the coarse level mesh for the refinement study, and factors of 1.4 and 2.0

would then be applied to consistently refine all zones within the domain.

Unstructured mesh generation for the C608 followed a workflow similar to the procedure outlined for the biconvex geometry. Star-CCM+ was again utilized to build the arbitrary polyhedral volume mesh which consisted of a prismatic layer extruded from all wall boundaries which transition to arbitrary polyhedral cells in the farfield. The domain extent and areas of local refinement including the engine exhaust wake and high-grdient regions were very consistent with the structured overset grid system. The resulting unstructured mesh is given in Fig. 15 presenting the surface and volume mesh characteristics. Final mesh statistics for the structured overset and unstructured polyhedral meshes are provided in Table 4.

**Table 4. Computational mesh statistics for the C608 geometry**

| Mesh | Total Nodes/Cells (M) | Total Degrees of Freedom (M) |
|---|---|---|
| Structured overset (coarse) | 51.472 | 40.335 |
| Structured overset (medium) | 161.990 | 127.379 |
| Structured overset (fine) | 558.092 | 450.919 |
| Unstructured polyhedral (coarse) | 27.685 | – |
| Unstructured polyhedral (medium) | 94.390 | – |
| Unstructured polyhedral (fine) | 140.333 | – |

### IV.F. Nearfield Pressure Signature Results

The curvilinear and unstructured methodology for simulating the C608 mesh refinement study applied many lessons learned from the biconvex shock-plume interaction model, with additional consideration given to added flow field complexity. Similar to the biconvex case, the subsonic regions of the domain within the internal flow passages posed challenges while determining a best-practice for obtaining steady-state convergence. Initializing all nodes/cells inside these internal flow paths to a subsonic state while initializing the rest of the domain to the specified supersonic freestream condition was found to be an effective approach. This accelerated the steady-state convergence while also ensuring the local flow field would remain in the correct sonic regime. Mach numbers provided by the workshop committee were used to compute a reasonable subsonic state for initialization. Furthermore, as was done for the biconvex case, the solution was initialized with a boundary layer at all viscous walls, in which the freestream velocity components are scaled linearly to zero over a specified off-wall height. Once a steady-state solution was obtained with the coarse level mesh, this solution was then interpolated onto the medium and fine resolution meshes, where any nodes unable to receive a donor would receive the freestream state. The medium and fine meshes were then initialized from this interpolated solution. Initializing the CFL number at 2.0 during the start-up transients and limiting the CFL to 150.0 worked well for this application across all refinement levels. Although the workshop provided two options for prescribing the ECS inlet and engine fan face inlet boundary, the authors of this paper elected to treat these outflow as a fixed static pressure boundary for all LAVA Curvilinear simulations presented.

The setup of the unstructured followed closely to that of the structured code. The flow around the aircraft was initialized using a similar artifical boundarly layer estimate and the various propulsion inflows and outflows were modeled by either back stagnation conditions or back pressures respectively. The only exception to this was the ECS inlet face. The unstructured solver has the option of specifying an average Mach number at a face for a boundary condition. Since the workshop committee provided both a back pressure and a Mach number, both types were tested and the results compared against each other.

A sample pressure slice near the symmetry plane in Fig. 16 provides an illustration of the computational domain extent and a visual of the nearfield on-track extraction location used for C608 nearfield analysis. The shock features captured in the domain extend to the farfield without any influence or dissipation induced by these boundaries, providing confidence that the computational mesh is sufficient to solve the nearfield problem without any unwanted artifacts. Furthermore, the wing tip vortices captured in Fig. 17 provided additional assurance that the mesh is sufficiently fine to capture relatively sophisticated flow structures without the need for any mesh adaptation methods. Distinct vortices produced by the wing, horizontal tail, and T-tail are shown to propagate well downstream of the vehicle, providing confidence that dissipation due to mesh coarsening or numerical discretization is minimal.

Computational resource usage for the mesh refinement study cases is compared for each solver and simulation approach used in Table 5. Also included for comparison are resources utilized for LAVA Curvilinear

simulations for the C608 case prior to refactoring the solver. As discussed in Subsection IV.C, the implementation of the GMRES linear solver, the ability to initialize simulations with previously computed solution on a different mesh, and other improvements yielded a 12-14X reduction in resource usage for the LAVA Curvilinear computations. Although results obtained from the original LAVA Curvilinear solver will only be briefly discussed here, verification was performed to ensure both variants of the curvilinear solver yielded consistent results. LAVA Unstructured resource usage is also provided for the refinement study where both methods of ECS and engine fan face outflow treatment (fixed static pressure and fixed Mach number) required the same amount of resources. All curvilinear simulations for the C608 refinement study were run using the modified Roe scheme, while all unstructured simulations were run with the AUSMPW+ scheme.

**Table 5. Resource usage for each C608 simulation in CPU-hours with SBUs (Standard Billing Units on the Pleiades and Electra supercomputers depending on node type used) provided in parentheses.**

| Solver (Scheme) | Coarse | Medium | Fine |
|---|---|---|---|
| LAVA Curvilinear, original (Roe) | 2,400 (79.2) | 7,680 (253.4) | 23,440 (773.5) |
| LAVA Curvilinear, refactored (Roe) | 160 (6.36) | 460 (18.3) | 1,800 (59.4) |
| LAVA Unstructured (AUSMPW+) | 2,352 (84.0) | 4,256 (152.0) | 7,000 (250.0) |

Figure 18 provides a comparison of the coarse, medium and fine resolution pressure signatures at the radial location $R = 3L$ from $X = 2,959in$ to $X = 5,011in$, corresponding to $X = -216in$ to $X = 1,836in$ at the aircraft location. Mesh refinement signatures are pictured for the on-track position, $\phi = 0$, and the conclusions discussed here are generally valid for all off-track positions. The curvilinear predictions in Fig. 18(a) appear to asymptotically converge towards the fine mesh solution as the meshes are refined, however all levels appear to sufficiently capture all key features at consistent locations. Local extrema as shown by the magnified regions are captured well by all mesh levels, with all maxima and minima locations predicted within two inches between the medium and fine resolutions. A wider spread in the signatures is observed at the aft end as expected, where steady-state RANS calculations might not be sufficient fidelity to capture shock-plume interaction physics. Unstructured predictions in Fig. 18(b) on all mesh levels capture consistent shock features across the signature, with similar slight differences noted between the medium and fine meshes. Extra sharpness in the fine mesh peaks, particularly at the canard and wing shock locations, is due to these shocks aligning more closely to mesh cells in the Mach-cone extruded portion of the mesh. Greater sensitivity is observed in the unstructured solutions when Mach number is prescribed at the ECS inlet and engine fan face inlet as opposed to static pressure, shown in Fig. 18(c). This is particularly true in the second to final overpressure peak in the front half of the signature, which is greatly influenced by the treatment of this outflow boundary condition. While the coarse mesh extrema are predicted relatively close to the medium and fine predictions using the static pressure boundary condition, these extrema magnitudes are dissipated considerably in the coarse solution compared to the medium and fine.

Pressure signatures at five azimuthal angles from $\phi = 0°$ to $\phi = 40°$ in increments of $10°$ are presented and compared for all LAVA fine mesh results alongside the ensemble mean computed from all workshop submissions, shown in Fig. 19. Overall, all shock features are predicted at locations consistent with the average data, while local maxima and minima are predicted near the mean value in most locations with higher peaks in various locations. The overpressure peaks in the front half of the signature are consistent with the mean, particularly between both solutions that utilized the fixed pressure boundary condition at the outflows. Near the shock structures created by the ECS inlet, the unstructured fixed Mach number signature creates noticeably larger peaks and troughs, particularly at lower off-track positions. Because the prescribed Mach number is much lower than the average Mach number computed at the ECS inlet when static pressure is fixed, this increased flow deceleration results in a stronger shock feature that persists from the on-track position to around $\phi = 45°$. This impacts of this shock are effectively localized to this location, where minor differences are noted in other locations downstream. Near the aft end of the signatures, other notable differences arise near the shock-plume interaction segment, where the final peaks due the aft deck and T-tail sections are predicted slightly upstream by the curvilinear solver relative to the unstructured solutions. Similar observations can be made across the other off-track positions, while the agreement appears to improve at higher azimuthal locations.The source of these differences will be discussed later as computed sound levels are compared, demonstrating the net effect that these differences can have when propagated. Figures 20 and 21 provide a final comparison across the complete carpet for the three codes and confirms there are no unexpected peculiarities in the signature predictions. Both codes appear to capture overpressure and

underpressure peaks consistently at all azimuths, with the structured code predicting slightly more resolved features at off-track positions between the $\phi = 90°$ to $\phi = 180°$ range.

Final comparisons of total loudness were made by using these nearfield signatures to compute the perceived level of noise (PL) and A-weighted sound exposure level (ASEL), a procedure which was performed by the workshop committee. These loudness metrics are commonly used to assess boom strength, and tend to be highly sensitive to overpressure and underpressure predictions in the vicinity of the aircraft. Figure 22 provides examples of sensitivity for the computed PL and ASEL loudness observed across the structured and unstructured fine mesh solutions compared to the ensemble mean. Boundary condition treatment at outflow faces using the unstructured solver has a notable impact on computed loudness from the on-track position to about $\phi = 20°$ with a difference of about $1.5dB$ in most locations. The sound levels then merge at higher off-track positions once the influence of the ECS inlet diminishes. All solutions predict a downward trend in the loudness between $\phi = 10°$ and $\phi = 20°$, decreasing by about $2dB$ to the minimum loudness. However, the location of this initial drop in loudness and subsequent behavior at higher off-track angles appears to be highly sensitive to the discrepancies noted in the pressure signatures, particularly at the aft 25% of the signature in the shock-plume interaction region. The differences in loudness reach up to $2.0dB$ at some off-track locations.

To further investigate these differences the signatures were propagated using sBOOM internally. All of the signatures were propagated using a sampling frequency of 300kHz, standard atmosphere, and no wind. The signatures were also pre-processed to have additional zero-padding ahead of the nose shock and to have a linear ramp to zero starting from $X = 4,720in$ to allow for more consistent results from sBOOM. These parameters were decided on based on previous experience using sBOOM to perform these types of propagations for the X-59 project. Figure 23 shows the propagated ground signatures at two different off-track angles. At both angles, the decreased Mach number at the ECS inlet face is resulting in a significant change of the ground pressure between $Time = 30 - 40ms$. At the aft end of the signatures a significant difference is observed between the unstructured and curvilinear results between $Time = 90 - 110ms$. To better quantify how both of these features affect the predicted overall noise level, it is useful to look at the $ASEL$ build-up plots, shown in Fig. 24 as they more intuitively relate the overpressure wave to the loudness metric. This plot shows that, for $\phi = 0°$, the use of the fixed Mach boundary condition at the ECS inlet causes an increase of about $2.0dB$ that occurs between $Time = 30 - 40ms$. In the $\phi = 30°$ plot however, the effect is far less significant, leading to an increase of only about $0.5dB$.

In addition to the differences caused by the use of the fixed Mach boundary condition, there was a slight difference between both mesh topologies at the nose shock, $Time = 10ms$. In the $\phi = 0°$ case, there is a difference between both results of about $0.5dB$. For the $\phi = 30°$ results, however, both mesh paradigms are predicting the same loudness due to the nose. This is one demonstration of how sensitive the ground level noise is to slight changes in the near field pressure signatures. Another area of difference between both mesh paradigms was at the back end of the signature, near $Time = 100ms$. The unstructured and structured results have different behavior in their pressure rise which produces differences in the predicted noise. Interestingly, at $\phi = 0°$ the structured result has a much larger increase in the $ASEL$ metric than the unstructured results, but at $\phi = 30°$ this trend is reversed. This shows that while the ground signatures seem qualitatively similar for both positions, they lead to quantitatively different results. A plot of the $\Delta p/P_\infty$ field on the symmetry plane shown in Fig. 25 was used to trace the source of the differences between both mesh types. From this comparison, it was observed that the interaction of the expansion from the trailing edge of the T-tail and the plume (emphasized in the black boxes) were showing significantly different pressure disturbance magnitudes. This difference in the behavior in the vicinity of the aircraft then propagates to the ground, which accounts for the majority of the difference in the predicted noise levels from the solvers. This implies that using steady-state RANS in this particular region of the flow field may not be capturing all of the relevant physics. In addition to the modeling uncertainty in this region, Fig. 25 shows that spacial discretization may also be contributing to the differences in the solutions. Both of the grids are shown in the figure. The fine grid from the structured grid being so fine that it is difficult to see the mesh lines in the image where the mesh is more easily seen in the unstructured image. The sensitivity seen between both solutions within LAVA agrees with what was seen in the workshop ensemble data. The shock-plume interaction region at the aft end of the signatures is the area of the largest sensitivity.

Despite this sensitivity, all sound levels predicted by LAVA fall within the one standard deviation of the ensemble mean at nearly every off-track position, with a few localized areas that peak outside of these bounds. It is critical to note that the ensemble data provided by the workshop is computed from the average

of 27 submissions, many of which were generated from meshes provided by the workshop. Therefore, this average most likely contains bias towards results computed on these meshes, contributing to the spread observed in the predictions. Overall, the spread observed in the loudness levels appears to stay within the general distribution observed during this workshop and past workshops as well, despite the added complexity of the geometry and inflow/outflow components.

### IV.G. Space Marching

An alternative approach to directly coupling the CFD near-field prediction to the far-field sonic boom propagation code sBOOM is to introduce an intermediate stage via space marching. An efficient high-order accurate Euler equation solver utilizing a space marching solution procedure was developed within LAVA.[7] By introducing the intermediate space marching layer, the CFD domain size can be dramatically reduced by more than eight body lengths for the C608 (assuming an sBOOM coupling location of $R/L_{body} = 3$ as used in the workshop). This reduction in CFD domain size reduces the overall cost of the CFD solution which represents more than 99 percent of the total computational cost for ground level noise prediction. The space marching procedure, on the other hand, only requires minutes on a workstation to propagate the solution from approximately the semi-span of the wing to tens of body lengths from the aircraft. This is equivalent to the cost of the far-field propagation code sBOOM which must be run for each azimuth independently. Moreover, the high-order space marching solver reduces potential errors in the near-field signatures predicted by standard second-order accurate CFD solvers on distorted Mach-cone aligned grids. The other major advantage of the space marching method is the ability to assess the sensitivity of the sBOOM coupling location to the ground level noise metric. Since far-field sonic boom propagation solvers utilize geometric acoustics and other simplifying assumptions, they can not account for the complex three-dimensional wave interaction effects such as azimuthal velocity dependence of the far-field noise. This will be demonstrated by using three different coupling locations, $R/L_{body} = 3$, 6, and 9. In fact, as the radial distance of the coupling location increases the benefit of using the space marching method within the ground level noise prediction procedure increases. This is because an increased radial distance in the coupling location would require a larger CFD mesh and thus an larger computational cost for the CFD solution. The space marching method utilizes the propagating direction in a time-like way, this implies that a larger radial coupling location can be viewed as solving an unsteady two-dimensional problem further in time, which only scales linearly with propagation distance.

Utilization of the space marching method is described in three sections. First, the reduced CFD domain size is described along with a comparison of the computational cost of the CFD solution on the reduced domain size, the original domain size used for the workshop, and a larger domain size utilized to assess the sensitivity of the radial coupling location with sBOOM. Next, the space marching grid and solver parameters used for this analysis are described and the space marching solution using the reduced CFD domain solution as input is compared to the large CFD domain solution at several on-track and off-track radial locations. Finally, the ground level noise predicted by coupling sBOOM to the space marching solution is compared to that computed using the CFD solution at two radial coupling locations, $R/L_{body} = 3$ and 6. The larger radial location requires a larger CFD domain than the one used in the workshop. An additional radial coupling location of $R/L_{body} = 9$ is also included using the space marching method to further illustrate the benefit of the using the method for ground level noise prediction.

#### *IV.G.1. Reduced CFD Domain*

A simple domain of dependence study was performed to determine the required radial extent of the CFD domain. This analysis consisted of constructing a forward opening Mach cone placed just upstream of the nose of the vehicle and a Mach cone opening in the opposite direction placed near the aft of the vehicle. The placement of these cones along the streamwise axis was adjusted until the entire vehicle geometry was encompassed by the two cones. The radius where the cones intersect, $R/L_{body} = 0.53$, provides a good estimate of the required radial domain extent. Figure 26 (a) shows the intersection of the two Mach cones along with the C608 vehicle located within the two cones. Results of the domain of dependence study were used to construct a modified off-body Mach cone aligned CFD grid script which allows the user to input the desired radial extent of the off-body grid. Figure 26 (b) shows the resulting off-body grids for the three radial CFD domain extents of interest; $R/L_{body} = 0.53$ the minimum required radial extent contains a total of 149 million grid points including the medium resolution near-body grids; $R/L_{body} = 4$ based on the workshop

specification of the sBOOM coupling at $R/L_{body} = 3$ which is now 178 million grid points; and $R/L_{body} = 7$ for sensitivity analysis of sBOOM coupling location at $R/L_{body} = 6$ which contains 203 million grid points. The $R/L_{body} = 0.53$ grid results in a 16 percent reduction in grid points compared to the $R/L_{body} = 4$ grid, and a 26.5 percent reduction compared to the $R/L_{body} = 7$ grid.

CFD solutions for the three grids were generated using the re-factored LAVA structured curvilinear overset grid solver. A comparison of the pressure field on a cylinder at $R/L_{body} = 0.25$ is plotted for the $R/L_{body} = 4$ and $R/L_{body} = 0.53$ in Figs. 27 (a) and (b) respectively. This location is near the coupling location of the space marching solver which will be described in more detail in the next section. There is no visible difference between the two solutions at the pressure scales included in the plots. This implies that the simplified domain of dependence study is sufficient for the C608 vehicle. Figure 27 (c) plots the residual convergence history as a function of wall-clock time. Each solution was run on 25 Broadwell nodes on NASA's Advanced Supercomputer Plieades. The CFD solver was run for a fixed 2000 iterations since machine convergence could not be achieved. The wall-clock time required for each radial domain extent was 109 minutes for $R/L_{body} = 7$, 93 minutes for $R/L_{body} = 4$, and 73 minutes for $R/L_{body} = 0.53$. The reduced CFD domain of $R/L_{body} = 0.53$ resulted in a 21.5 percent reduction in wall-clock time compared to the workshop specified radial extent of $R/L_{body} = 4$, and a 33 percent reduction for the larger radial extent of $R/L_{body} = 7$. Examining the on-track pressure signature at $R/L_{body} = 0.25$ in figure 27 (d) shows no difference in the pressure signatures. In the next next two sections the reduced CFD domain will be used as input into the space marching solver the resulting pressure field will be compared with the larger CFD domain results.

### *IV.G.2. Space Marching Grid and Solver Methodology*

The automatically generated Mach cone aligned space marching grid algorithm developed in Housman *et al.*[7] has been modified to enable valid space marching even when the local Mach approaches unity. Figure 28 (a)-(d) shows several views of a coarse grid version of the space marching grid. The radial domain extent was set to $R/L_{body} = 10$ to enable sBOOM coupling up to $R/L_{body} = 9$. The space marching direction is oriented in the streamwise direction and the solution starts at the first upstream plane and marches downstream. An elliptic hole cutting approach has been implemented to replace the cylindrical hole cutting in the original algorithm to allow closer coupling to the aircraft. The first three layers of nodes, denoted "fringe" points, are used to couple the CFD solution to the space marching grid. The fringe points are illustrated in the figure 28 (d), the CFD solution is interpolated at these locations and used as boundary conditions during the space marching solution procedure. Three space marching grid resolutions were generated with $\Delta s/L_{body} = 0.006$, 0.003, and 0.0015 which resulted in 18.9 million, 72.3 million, and 285.4 million grid points respectively.

The three-dimensional Euler equations are discretized using a fourth-order Hybrid Weighted Compact Nonlinear scheme with third-order WENO interpolation in the non-space marching direction, while a second order backward differencing scheme is used to discretize the equations in the space marching direction. The two-dimensional non-linear system is solved at each space marching station using an alternating line Jacobi relaxation procedure, and converged two orders of magnitude before marching to the next station. Details of the numerical discretization and implicit solution procedure are described in Housman *et al.*[7] For the three space marching grids used in this study, the space marching solution time required 44 seconds, 139 seconds, and 440 seconds respectively, using 80 OMP threads on a modern high-end workstation. These computational resources are negligible compared to the cost of the CFD even on the finest space marching grid.

### *IV.G.3. Space Marching Results*

In order establish to necessary mesh resolution for the space marching grid, the near-field pressure signatures are compared to the CFD solution. Figure 29 (a)-(d) plot the pressure signatures at $R/L_{body} = 3$ and 6 both on-track and off-track, $\phi = 30^\circ$ for the CFD as well of the three space marching grid resolutions considered. Noticeable differences between the CFD and the coarsest space marching grid resolution, $\Delta s/L_{body} = 0.006$, are observed. The medium and fine space marching grid resolutions, $\Delta s/L_{body} = 0.006$ and 0.0015 are essentially on-top of the CFD. An inset image of the wave-train created by the wing are included in each image. Examination of the inset images shows a minor discrepancy between the medium space marching grid resolution and the CFD. The fine space marching grid solution is indistinguishable from the CFD. From

this analysis, the $\Delta s/L_{body} = 0.0015$ space marching grid resolution is chosen for far-field propagation with sBOOM.

Three radial coupling locations were analyzed for coupling the space marching solution with sBOOM, $R/L_{body} = 3$, 6, and 9. The closer two locations were also propagated using the $R/L_{body} = 7$ CFD solution. Figure 30 (a) plots a comparison of the ground signatures using the space marching and CFD solutions coupled at $R/L_{body} = 3$. The two ground signatures are almost identical with only a minor discrepancy between $120 - 130$ ms. The difference in the perceived loudness (PL) level is 0.2 dB between the solutions with the space marching solution producing a PL of 77.9 dB and the CFD generating 77.7 dB. A similar comparison is shown in figure 30 (b) but with coupling location extended to $R/L_{body} = 6$. Again, there is almost no difference in the ground signatures with the same minor discrepancy between $120 - 130$ ms. As in the previous analysis, a 0.2 dB difference is observed in the PL but the levels are slightly elevated to a PL of 78 dB for space marching and 77.8 for CFD. This prompted additional analysis using the space marching solution and extending the coupling location to $R/L_{body} = 9$. Figure 30 (c) shows the ground signature generated for each of the coupling locations resulting in a PL of 78.1. Examining the ground signatures there is almost no difference between the $R/L_{body} = 6$ and 9, while a noticeable difference is observed when coupling at $R/L_{body} = 3$ between $112 - 137$ ms which coincides with the differences observed between space marching and CFD indicating strong sensitivity in this region. Moreover, the 0.1 dB incremental trend with increasing radial coupling location is also observed. Extended analysis comparing coupling locations starting at $R/L_{body} = 10$ and extending to 100 in one body length increments was performed and the increasing PL level trend persisted. This analysis is out of the scope of the current paper, but investigation into this behavior in collaboration with the developer of sBOOM is ongoing and will be reported in a future publication.

## V. Summary

The LAVA team has successfully completed all required analysis for the SPBW3 submission, and was also able to provide results using both the curvilinear and unstructured solvers within LAVA, helping to quantify uncertainty in CFD predictions. Developments and improvements made to the framework have also enabled the authors to produce CFD results at a fraction of the computational cost required in previous workshops. For example, compared to previous versions of the LAVA Curvilinear solver, a 3-15X savings in computational resources could be achieved using the refactored LAVA curvilinear solver for the biconvex shock-plume interaction and the C608 cases. Workshop results presented in this paper for the nearfield and farfield components of the workshop demonstrate the ability of the curvilinear, unstructured, and space marching solvers available in the LAVA framework to produce consistent CFD predictions in the low supersonic flow regime.

Nearfield workshop analysis was divided into the biconvex shock-plume interaction model and the C608 X-59 prototype, results of which were discussed at length. The biconvex subtask served as a useful validation case demonstrating LAVA's ability to make accurate CFD predictions for a generalized supersonic application. This effort also provided a baseline methodology for the CFD analysis of the more complex C608 supersonic aircraft workshop problem, among other considerations. Pressure disturbance predictions for the biconvex agree reasonably well with experimental data, with any error generally attributed to wind tunnel installation effects and reference condition drift not modeled in the CFD simulations. The C608 workshop subtask served to test LAVA's capability to compute consistent boom predictions for a geometry of interest to the aerospace industry. Many added layers of complexity were incorporated into this workshop analysis that had not been encountered in previous workshops. For instance, the inflow and outflow boundaries at the ECS inlet, engine fan face, engine exhaust, and engine bypass added additional sensitivity and uncertainty to an already complex problem from a geometric perspective. It was discovered that while the nearfield pressure signatures of interest exhibited strong consistency across the various solvers, small differences in local extrema predictions propagate into as much as 2.0 $dB$ differences in predicted sound levels. These differences were traced to discrepancies in pressure disturbance due to the aft shock-plume interaction region, the physics of which may not be accurately captured using a steady-state RANS approach and are highly sensitive to mesh treatment. Despite these differences, the variations observed within the LAVA solutions were never outliers relative to other workshop submissions, and almost all quantities assessed including $dP/P$ at all $\phi$, $PL$, and $ASEL$ were within one standard deviation of the ensemble mean.

An alternative three-step procedure to obtain ground level noise predictions using CFD, space marching,

and sBOOM was demonstrated. The three-step procedure was shown to be 21.5 to 33 percent less expensive than the traditional two-step CFD/sBOOM coupling, depending on radial coupling location, with no loss in accuracy. In fact, space marching was shown to be an economical approach to analyzing sensitivity to radial coupling location allowing an arbitrary radial distance to be space marched (provided atmospheric effects are negligible within this domain). The increase of speed using the three step procedure is expected to be even greater when coupling to unstructured CFD solvers which are typically on order of magnitude more computationally expensive than structured grid solvers for similar effective mesh resolutions.

**Acknowledgements**

Analysis to support the Sonic Boom Prediction Workshop was funded by the NASA Advanced Air Vehicles Program's Commercial Supersonic Technologies (CST) Project. Refactorization of the LAVA flow solver has been partially funded by the CST, the Transformational Tools and Technologies (TTT), and the Advanced Air Transport Technology (AATT) Projects. The authors would like to thank the organizing committee for the 3rd AIAA Sonic Boom Prediction Workshop for hosting the workshop, as well as Sriram Rallabhandi from NASA Langley Research Center for his assistance in training and familiarizing the LAVA team with sBOOM. The authors would also like to thank Mike Aftosmis from NASA Ames for providing the utilities that were used to create the *ASEL* build-up plots. Finally, the authors would like to thank the NASA Advanced Supercomputing (NAS) division at NASA Ames Research Center for providing the computing facilities used to complete this work.

## References

[1]Kiris, C., Housman, J., Barad, M., Brehm, C., Sozer, E., and Moini-Yekta, S., "Computational Framework for Launch, Ascent, and Vehicle Aerodynamics (LAVA)," *Aerospace Science and Technology*, Vol. 55, August 2016, pp. 189–219.

[2]Housman, J., Sozer, E., Moini-Yekta, S., and Kiris, C., "LAVA Simulations for the AIAA Sonic Boom Prediction Workshop," *32nd AIAA Applied Aerodynamics Conference, Atlanta, GA*, June 2014, AIAA-2014-2008.

[3]Cliff, S., Durston, D., Elmiligui, A., Jensen, J., and Chan, W., "Computational and Experimental Assessment of Models for the First AIAA Sonic Boom Prediction Workshop," *52nd Aerospace Sciences Meeting, National Harbor, Maryland*, January 2014, AIAA-2014-0560.

[4]Durston, D., e. a., "Nozzle Plume/Shock Interaction Sonic Boom Test Results from the NASA Ames 9- by 7-Foot Supersonic Wind Tunnel," *55th Aerospace Sciences Meeting, Grapevine, Texas, Jan 5, 2017*, January 2017, AIAA-2014-0041.

[5]Durston, D. A., Cliff, S. E., Denison, M. F., Jensen, J. C., Moran, P. J., Smith, N. T., Heineck, J. T., Schairer, E. T., Kushner, L. K., Castner, R. S., et al., "Nozzle Plume/Shock Interaction Experimental and Computational Sonic Boom Analyses from the NASA Ames 9-by 7-Foot Supersonic Wind Tunnel," 2018.

[6]Rallabhandi, S. K., "Advanced Sonic Boom Prediction Using the Augmented Burgers Equation," *Journal of Aircraft*, Vol. 48, No. 4, 2011, pp. 1245–1253.

[7]Housman, J. A., Kenway, G. K., Jensen, J. C., and Kiris, C. C., "Efficient Near-Field to Mid-Field Sonic Boom Propagation using a High-Order Space Marching Method," *AIAA Aviation 2019 Forum*, 2019, p. 3487.

[8]Deng, X., Mao, M., Jiang, Y., and Liu, H., "New High-Order Hybrid Cell-Edge and Cell-Node Weighted Compact Nonlinear Schemes," *20th AIAA Computational Fluid Dynamics Conference, Honolulu, Hawaii*, June 2011, AIAA-2011-3857.

[9]Kim, K. H., Kim, C., and Rho, O.-H., "Methods for the Accurate Computations of Hypersonic Flows: I. AUSMPW+ Scheme," *Journal of Computational Physics*, Vol. 174, November 2001, pp. 38–80.

[10]Spalart, S. and Allmaras, S., "A One-Equation Turbulence Model for Aerodynamic Flows," *30th Aerospace Sciences Meeting and Exhibit, Reno, NV*, January 1992, AIAA-92-0439.

[11]Menter, F. R., "Two-equation eddy-viscosity turbulence models for engineering applications," *AIAA journal*, Vol. 32, No. 8, 1994, pp. 1598–1605.

[12]Shur, M. L., Strelets, M. K., Travin, A. K., and Spalart, P. R., "Turbulence Modeling in Rotating and Curved Channels: Assessing the Spalart-Shur Correction," *AIAA Journal*, Vol. 38, No. 5, 2000, pp. 784–792.

[13]Spalart, P. R., "Strategies for Turbulence Modeling Simulations," *International Journal of Heat and Fluid Flow*, Vol. 21, 2000, pp. 252–263.

[14]Saad, Y. and Schultz, M. H., "GMRES: A generalized minimal residual algorithm for solving nonsymmetric linear systems," *SIAM Journal on scientific and statistical computing*, Vol. 7, No. 3, 1986, pp. 856–869.

[15]BETA-CAE, "ANSA Pre-processor, The Advanced CAE Pre-processing Software for Complete Model Build-up," 2019, http://www.beta-cae.com/ansa.htm.

[16]Pointwise, "Grid Generation Software," https://https://www.pointwise.com.

[17]Park, M. A. and Nemec, M., "Nearfield Summary and Statistical Analysis of the Second AIAA Sonic Boom Prediction Workshop," *Journal of Aircraft*, Vol. 56, No. 3, 2019, pp. 851–875.

[18]Chan, W., "Developments in Strategies and Software Tools for Overset Structured Grid Generation and Connectivity," *20th AIAA Computational Fluid Dynamics Conference, Honolulu, Hawaii*, June 2011, AIAA-2011-3051.

[19]Park, M., Campbell, R., Elmiligui, A., Cliff, S., and Nayani, S., "Specialized CFD Grid Generation Methods for Near-Field Sonic Boom Prediction," *52nd AIAA Aerospace Sciences Meeting, National Harbor, Maryland*, January 2014, AIAA-2014-0368.

[20]Nichols, R. H. and Buning, P. G., *User's Manual for OVERFLOW 2.2*, NASA, March 12, 2019 (accessed June, 2019).

[21]Siemens, "Simcenter Star-CCM+," 2018, www.cd-adapco.com/products/star-ccm.

[22]Shur, M. L., Spalart, P. R., Strelets, M. K., and Travin, A. K., "A hybrid RANS-LES approach with delayed-DES and wall-modelled LES capabilities," *International Journal of Heat and Fluid Flow*, Vol. 29, No. 6, 2008, pp. 1638–1649.

[23]Jensen, J. C., Denison, M., Durston, D., and Cliff, S. E., "Computational Evaluations of Experimental Data for Sonic Boom Models with Nozzle Jet Flow Interactions," *55th AIAA Aerospace Sciences Meeting*, 2017, p. 0042.

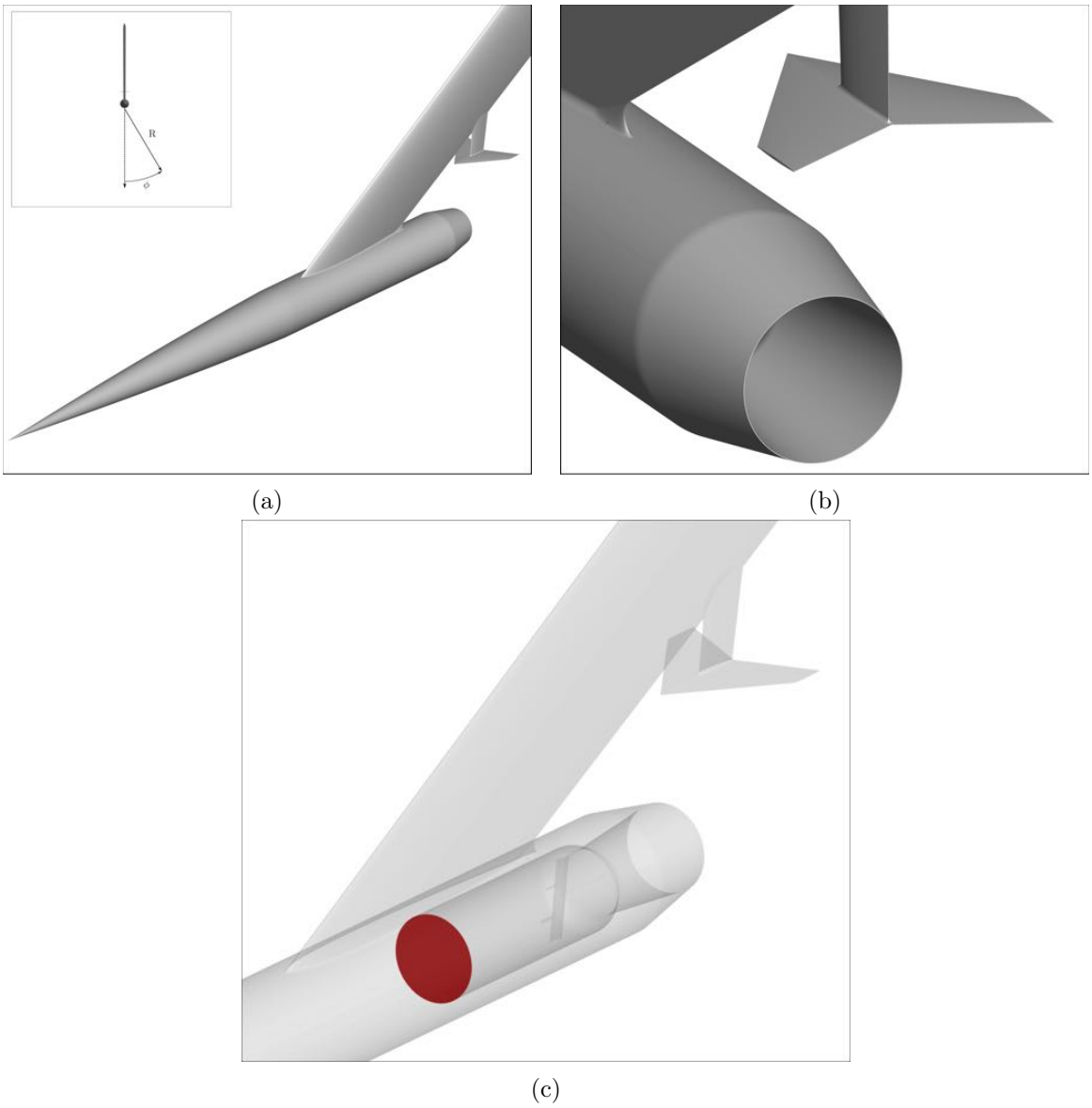



**Figure 1. (a) Isometric view of the biconvex shock-plume interaction CAD model. (b) Rear enhanced view of the biconvex T-tail geometry. (c) Transparent isometric view of the biconvex and nozzle, with the red surface indicating the nozzle inflow face.**

Biconvex Images

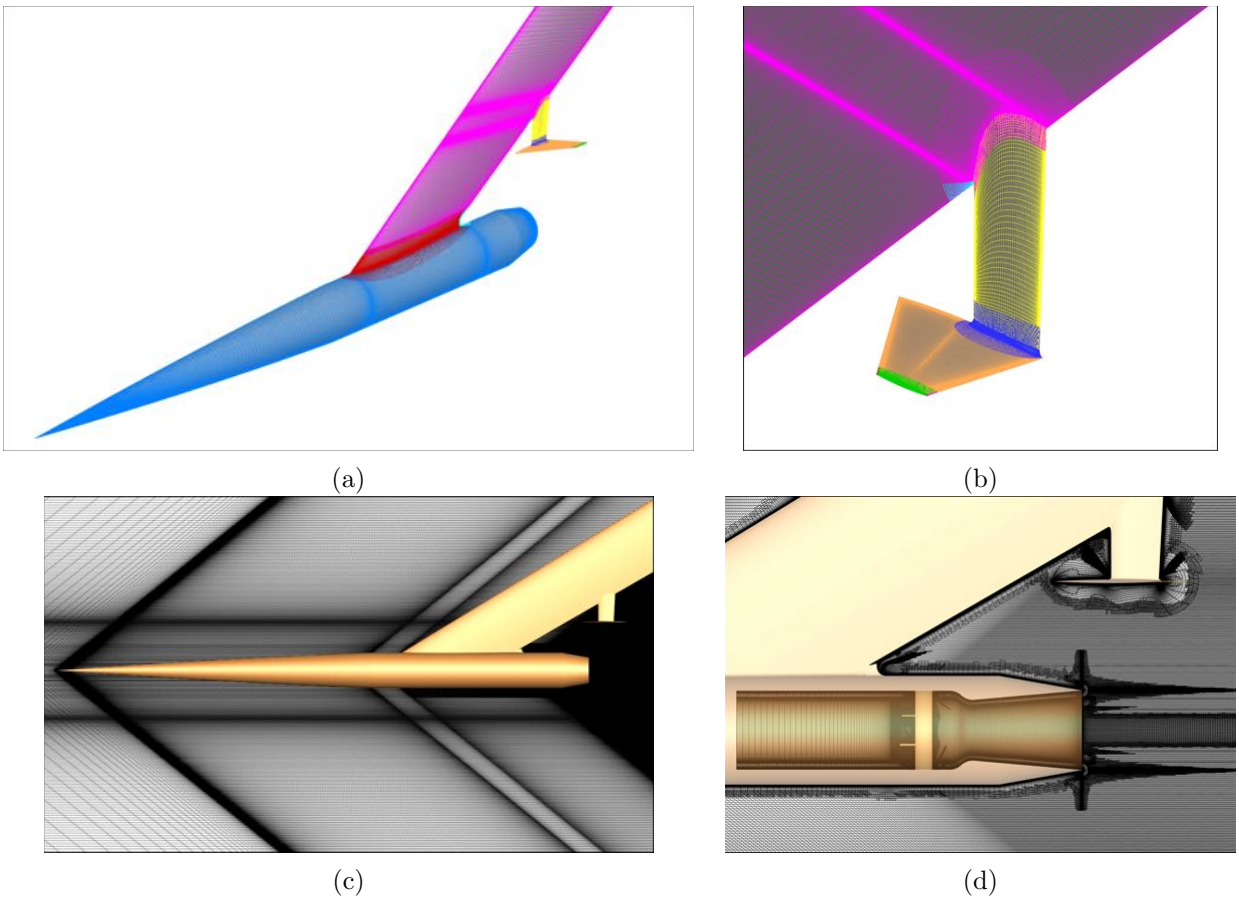
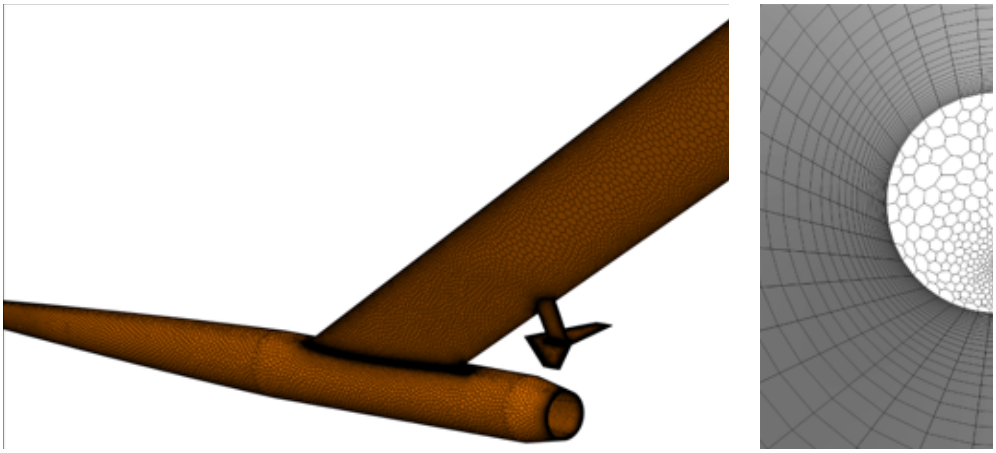
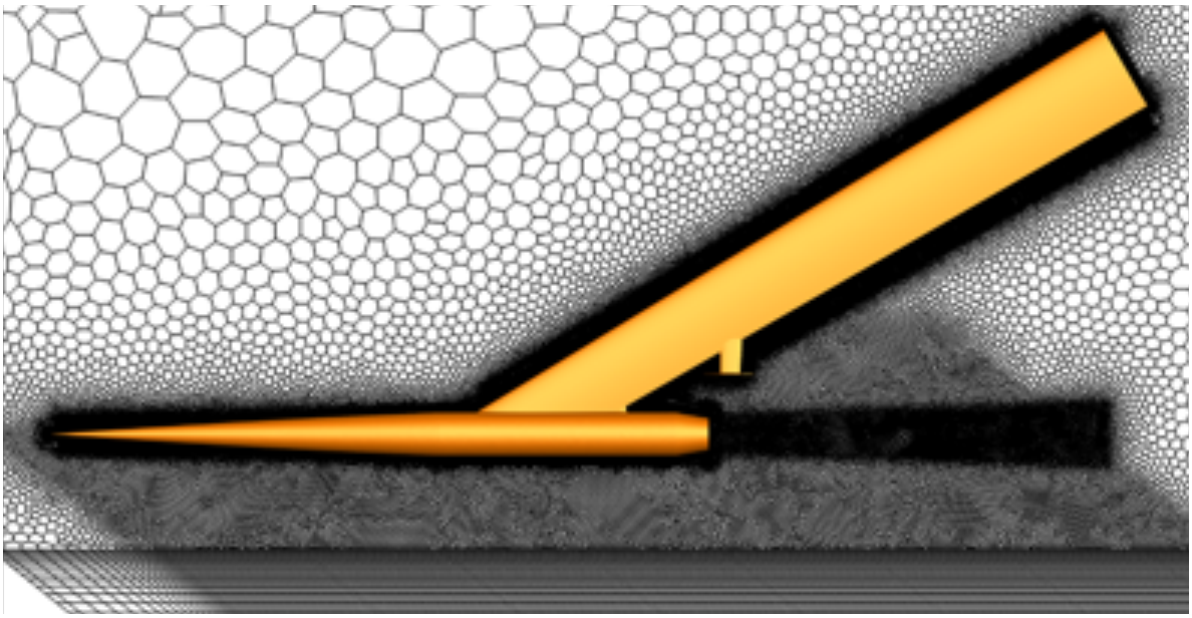



**Figure 2. (a) Isometric view of the biconvex shock-plume model structured overset computational mesh. (b) Close-up view of the biconvex T-tail section mesh. (c) Slice of the Mach-aligned computational grid at the model symmetry plane, with a close-up view at the nozzle exit and nozzle interior given in (d).**



(a) (b)



(c)

**Figure 3. (a) Isometric view of the unstructured arbitrary polyhedral computational mesh. (b) Close-up of the cylindrical core mesh and Mach-aligned extrusion layers. (c) Slice through the volume mesh at the model symmetry plane.**

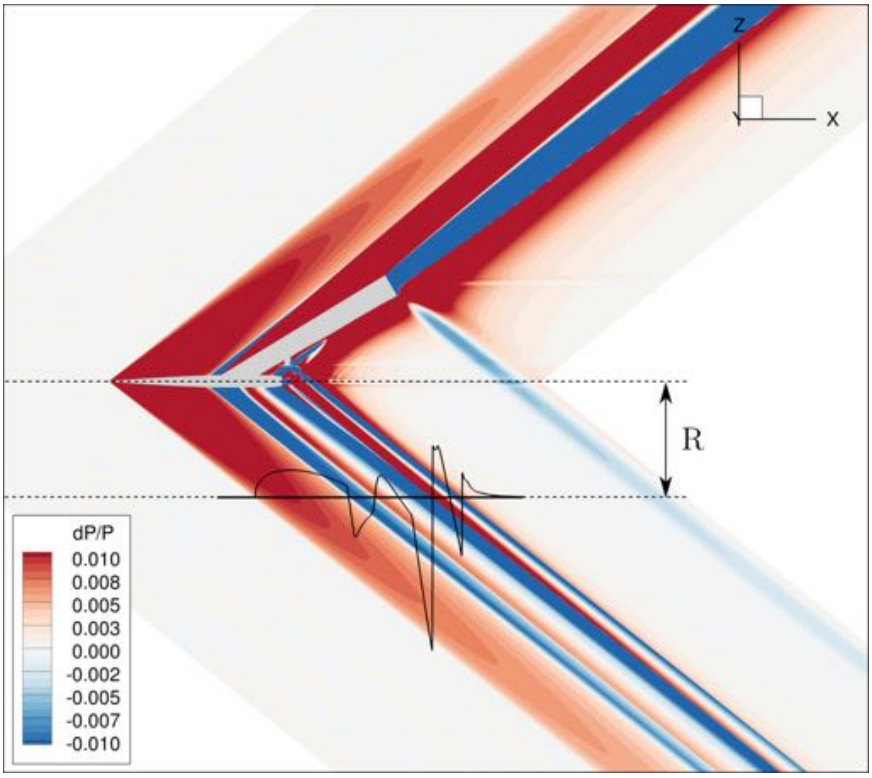



**Figure 4. Sample pressure disturbance at model symmetry plane with sample pressure signature extraction shown at the nearfield location of all workshop comparisons, $R = 15.1in.$**

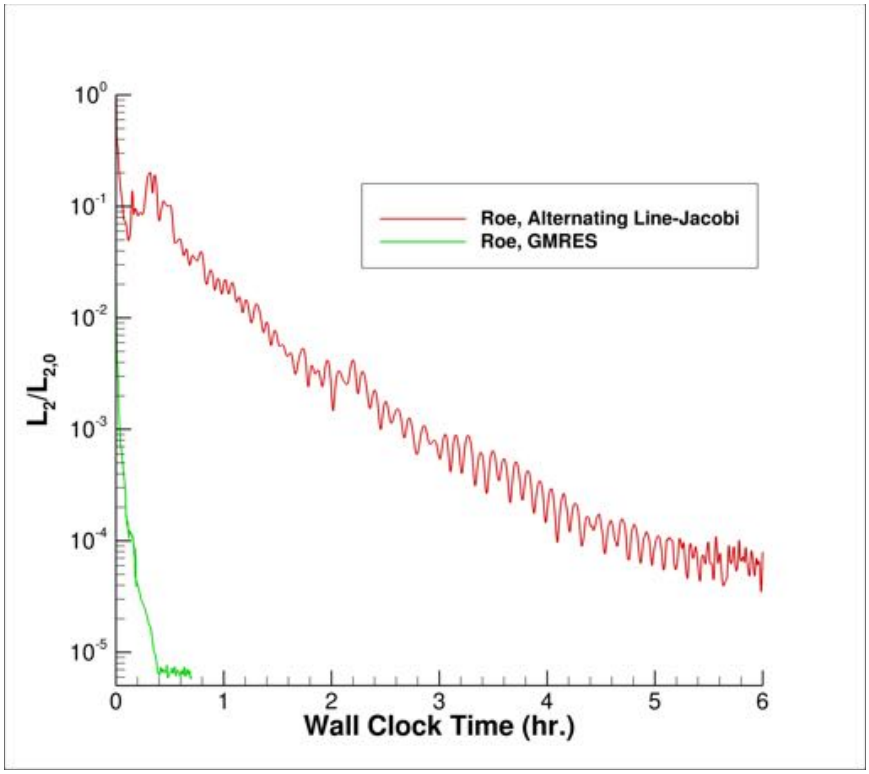



**Figure 5. (a) Normalized $L_2$ norm of the mean flow RANS equation residuals for the Alternating Line-Jacobi and GMRES linear solver for the modified Roe scheme.**

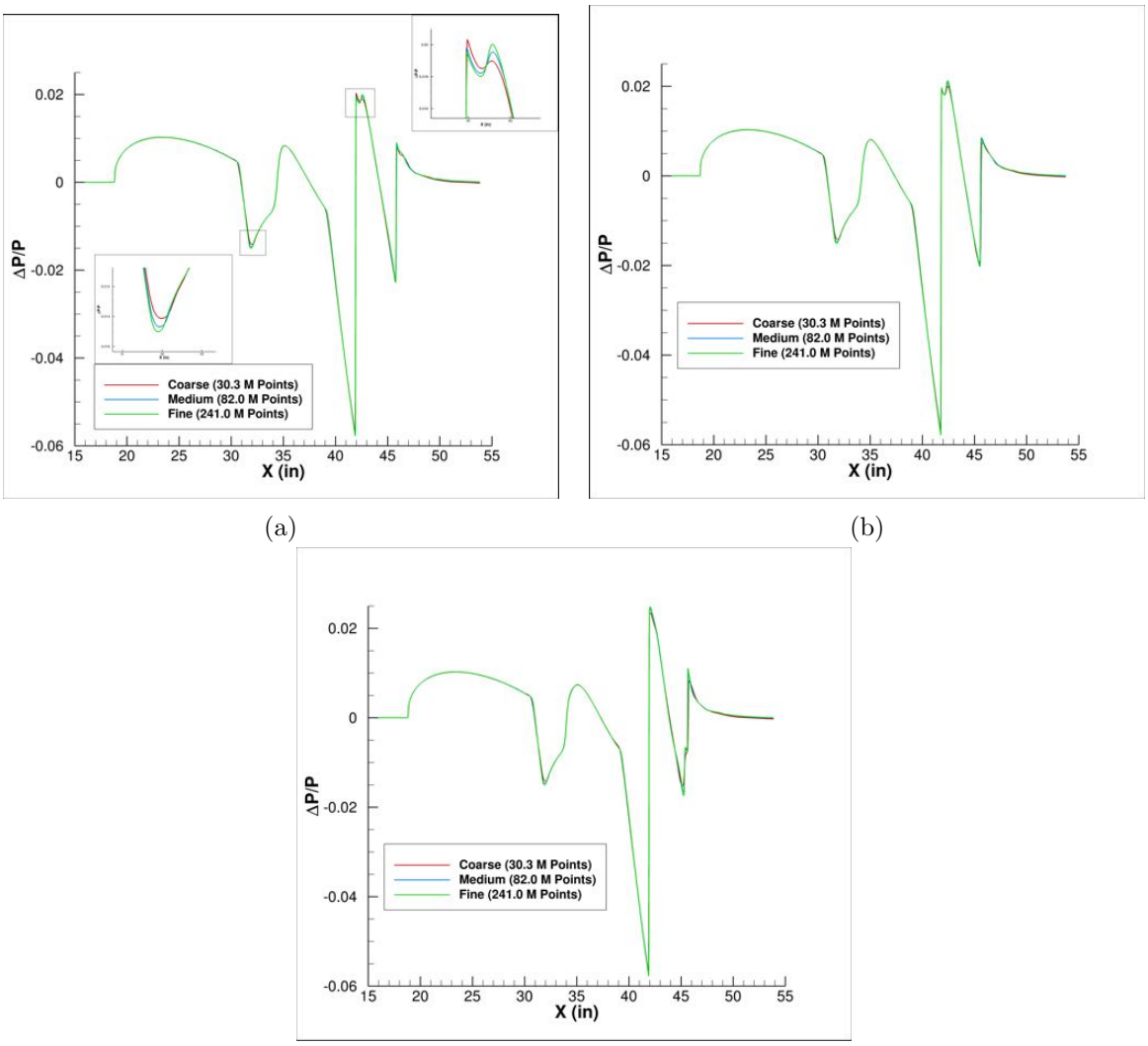



**Figure 6. Pressure signatures extracted from the LAVA Curvilinear mesh refinement solutions using the modified Roe scheme at $R = -15.1in.$ corresponding to axial model locations $X = -5.0in.$ to $X = 35.0in.$ for azimuthal positions (a) $\phi = 0.0^{\circ}$, (b) $\phi = 15.0^{\circ}$, and (c) (a) $\phi = 30.0^{\circ}$.**

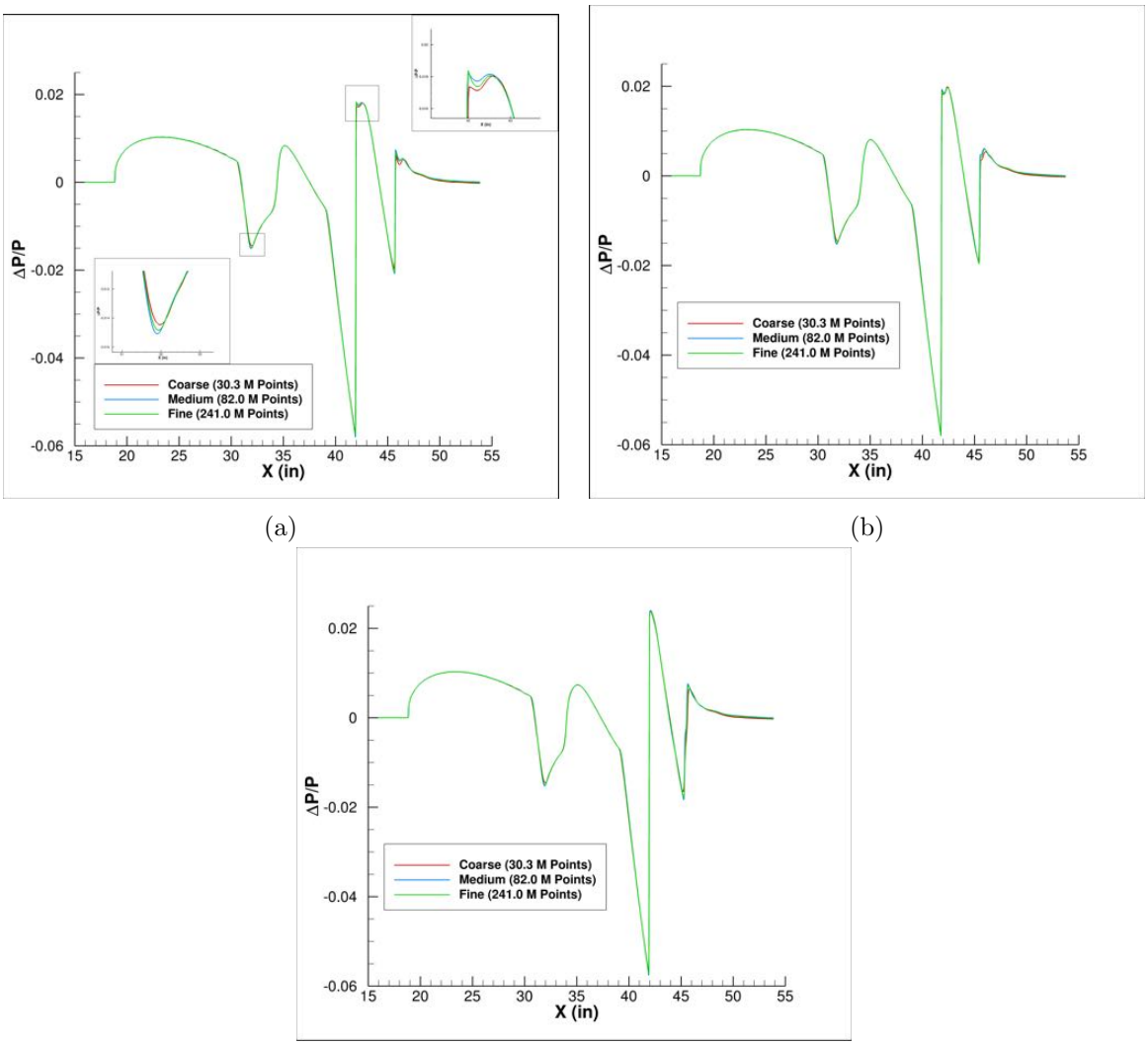
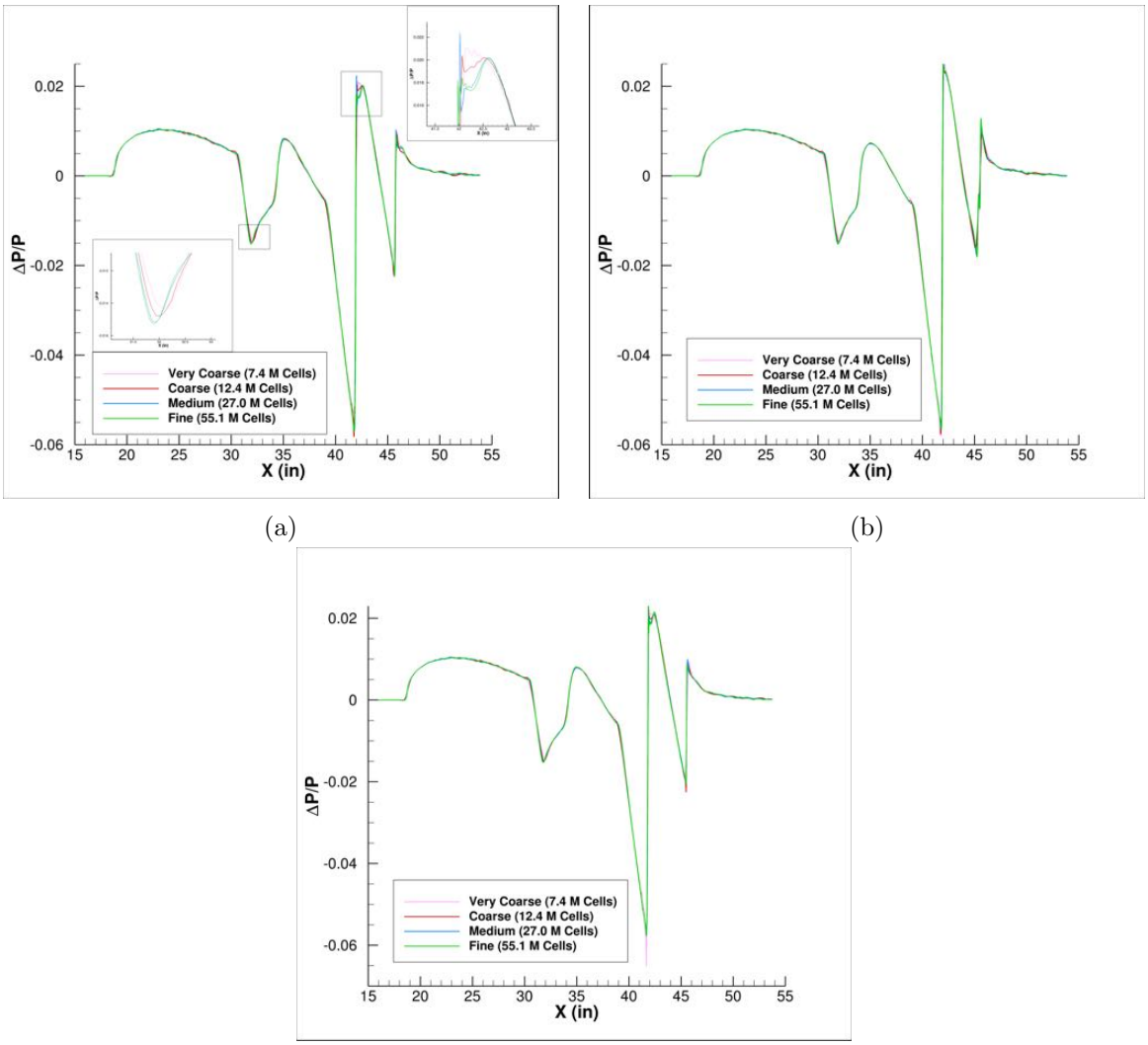



**Figure 7. Pressure signatures extracted from the LAVA Curvilinear mesh refinement solutions using the HWCNS scheme at $R = -15.1in.$ corresponding to axial model locations $X = -5.0in.$ to $X = 35.0in.$ for azimuthal positions (a) $\phi = 0.0^{\circ}$, (b) $\phi = 15.0^{\circ}$, and (c) (a) $\phi = 30.0^{\circ}$.**




(a) (b)

(c)

**Figure 8. Pressure signatures extracted from the LAVA Unstructured mesh refinement solutions using the AUSMPW+ scheme at $R = -15.1in.$ corresponding to axial model locations $X = -5.0in.$ to $X = 35.0in.$ for azimuthal positions (a) $\phi = 0.0^\circ$, (b) $\phi = 15.0^\circ$, and (c) (a) $\phi = 30.0^\circ$.**

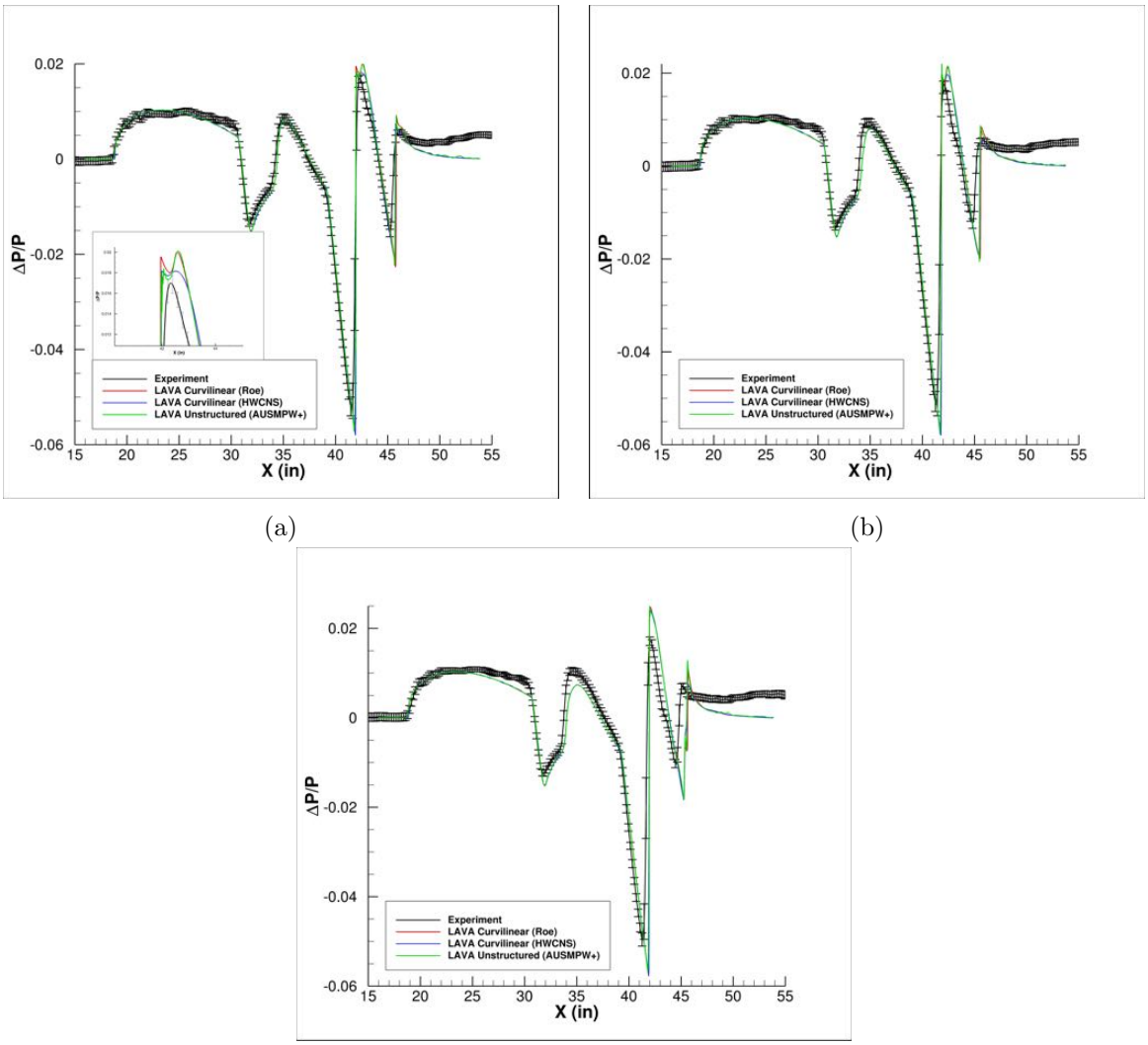



**Figure 9. Pressure signatures extracted at $R = -15.1in.$ for all LAVA simulations compared to experimental data gathered in the 9- by 7-ft. Supersonic Wind Tunnel. Axial locations sampled correspond to model locations $X = -5.0in.$ to $X = 35.0in.$ for azimuthal positions (a) $\phi = 0.0^\circ$, (b) $\phi = 15.0^\circ$, and (c) (a) $\phi = 30.0^\circ$.**

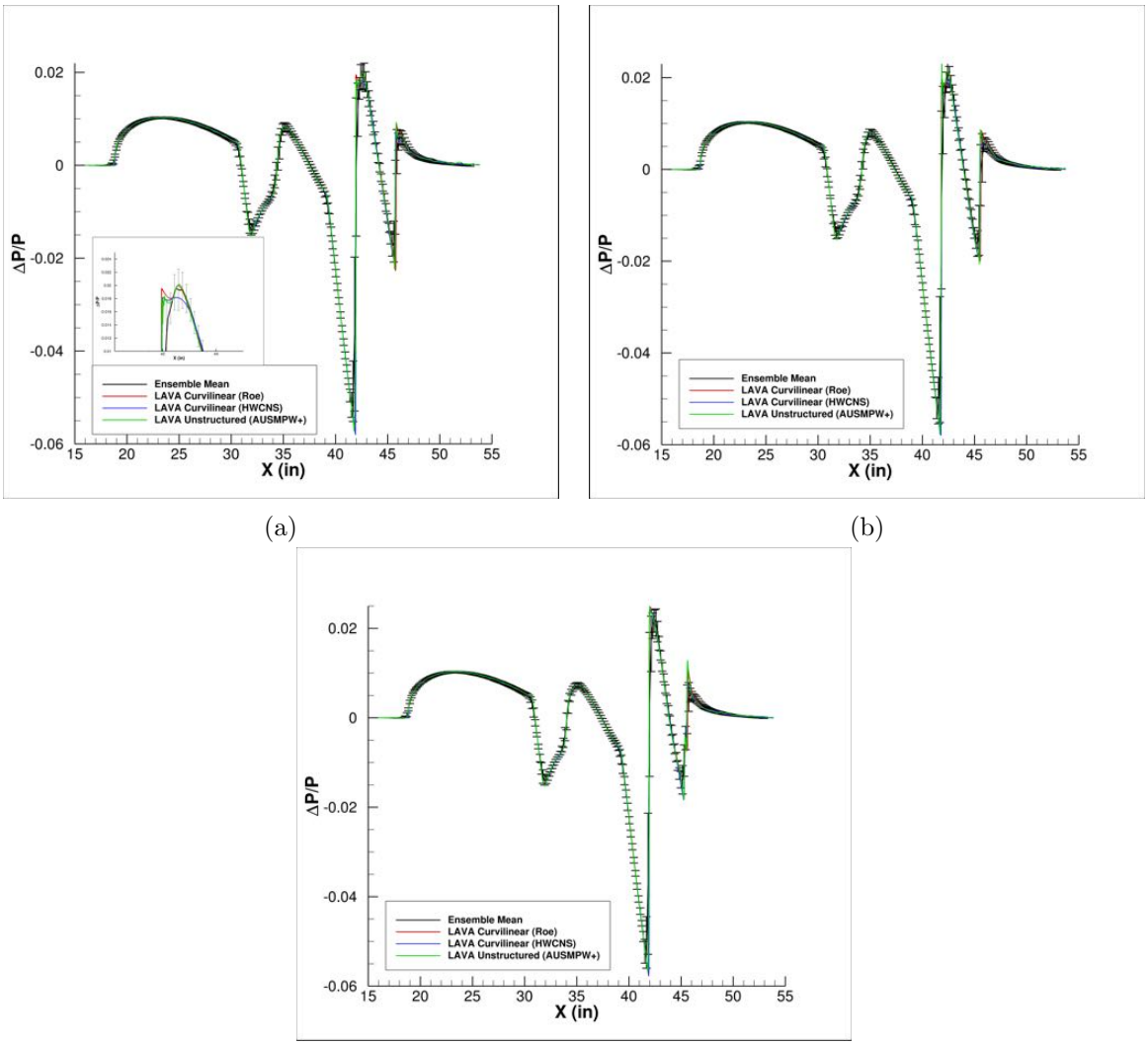
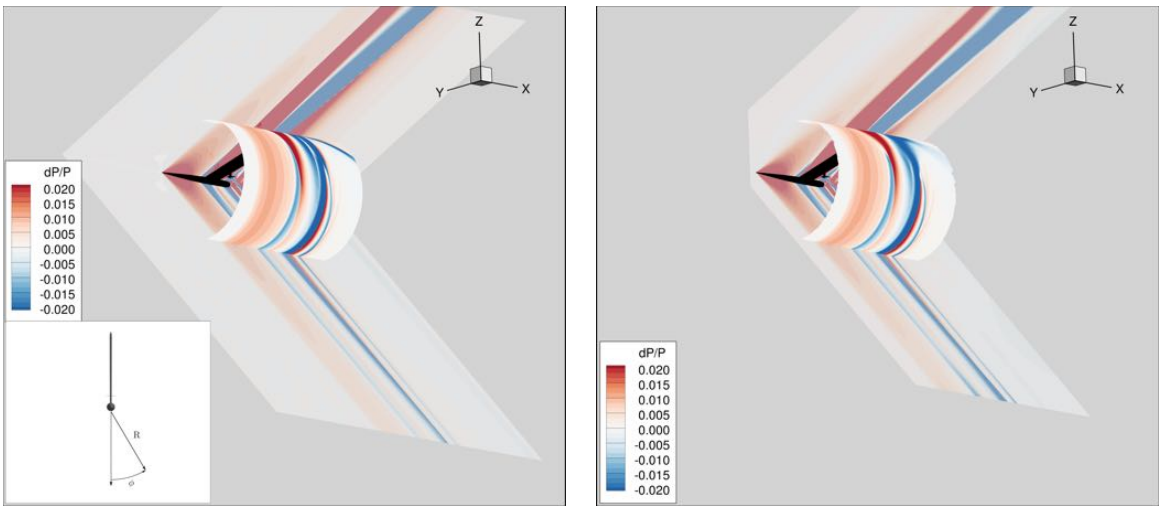



**Figure 10. Pressure signatures extracted at $R = -15.1in.$ for all LAVA simulations compared to the ensemble average of all workshop submissions. Axial locations sampled correspond to model locations $X = -5.0in.$ to $X = 35.0in.$ for azimuthal positions (a) $\phi = 0.0^\circ$, (b) $\phi = 15.0^\circ$, and (c) (a) $\phi = 30.0^\circ$.**




(a) (b)

**Figure 11. Pressure disturbance boom carpet contours at $R = 15.1in.$ with a solution slice through the model symmetry plane for the (a) LAVA Curvilinear modified Roe scheme solution (b) LAVA Unstructured solution using the AUSMPW+ scheme.**

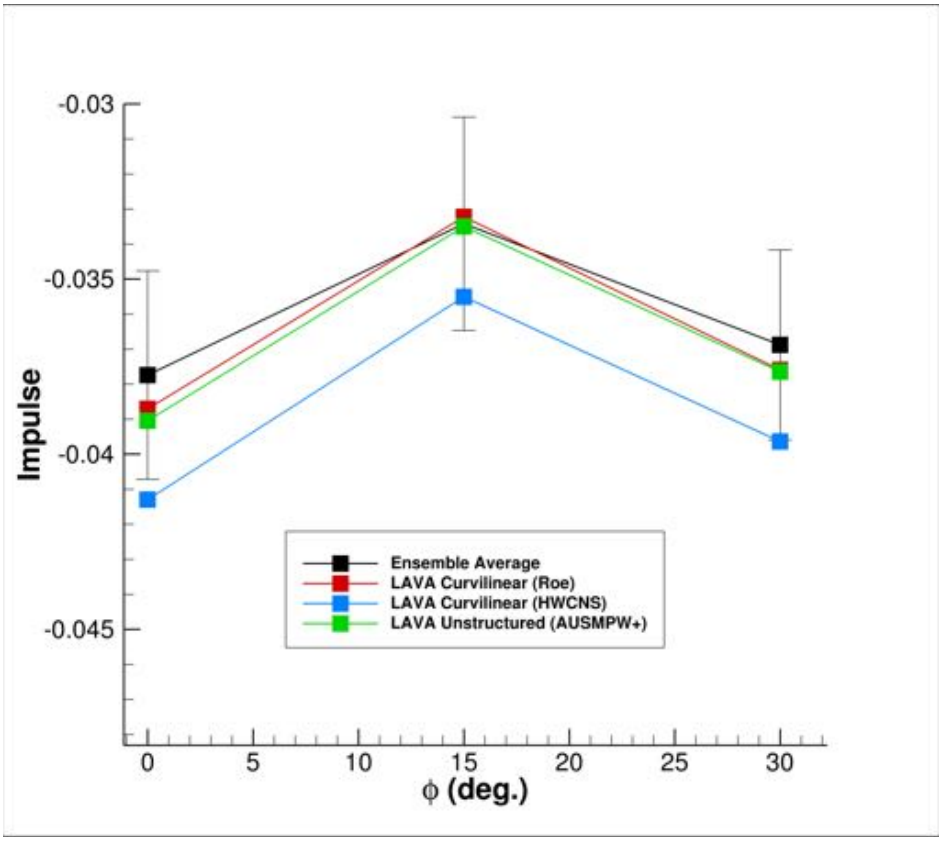
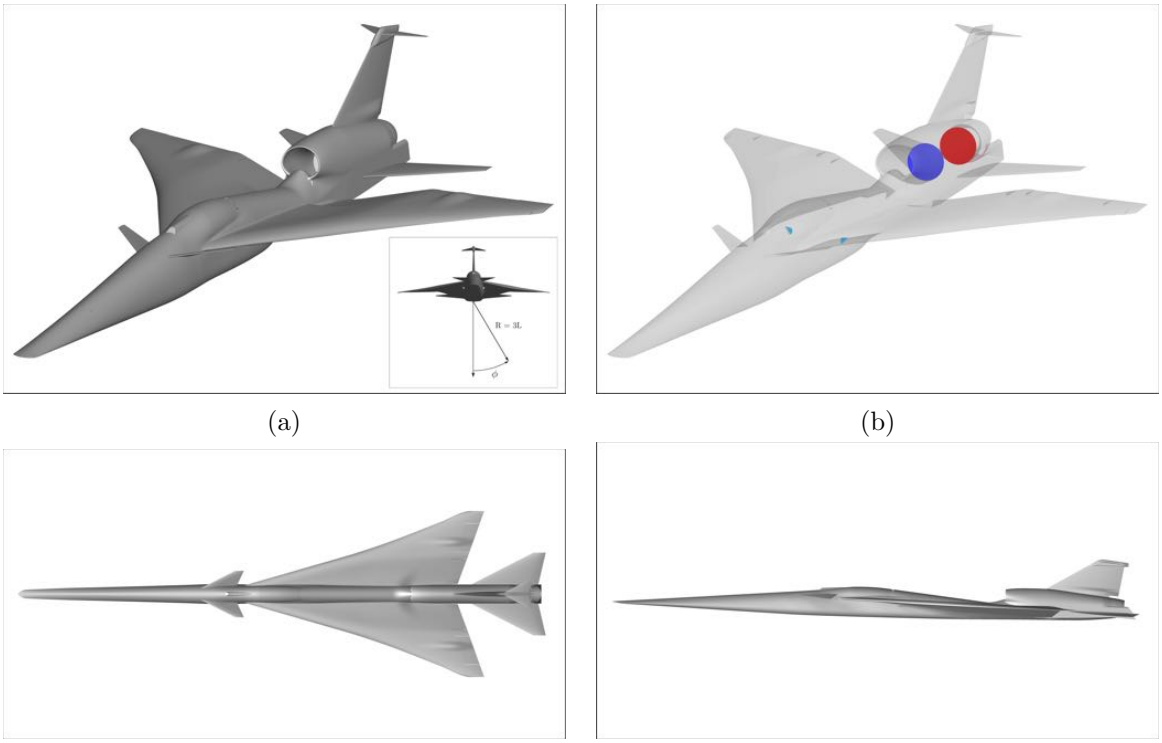



**Figure 12. Impulse computed for the nozzle lip region of the biconvex model for all solutions compared to the ensemble average of all workshop submissions.**



(a) (b)

(c) (d)

**Figure 13. (a) Isometric view of the c608 supersonic aircraft CAD model. (b) Transparent isometric view with subsonic inflow and outflow boundaries colored, cyan showing the ECS inlet, blue showing the engine fan face inlet, red showing the engine exhaust outlet, and magenta showing the engine bypass outlet. Additional top view (c) and side view (d) also provided.**

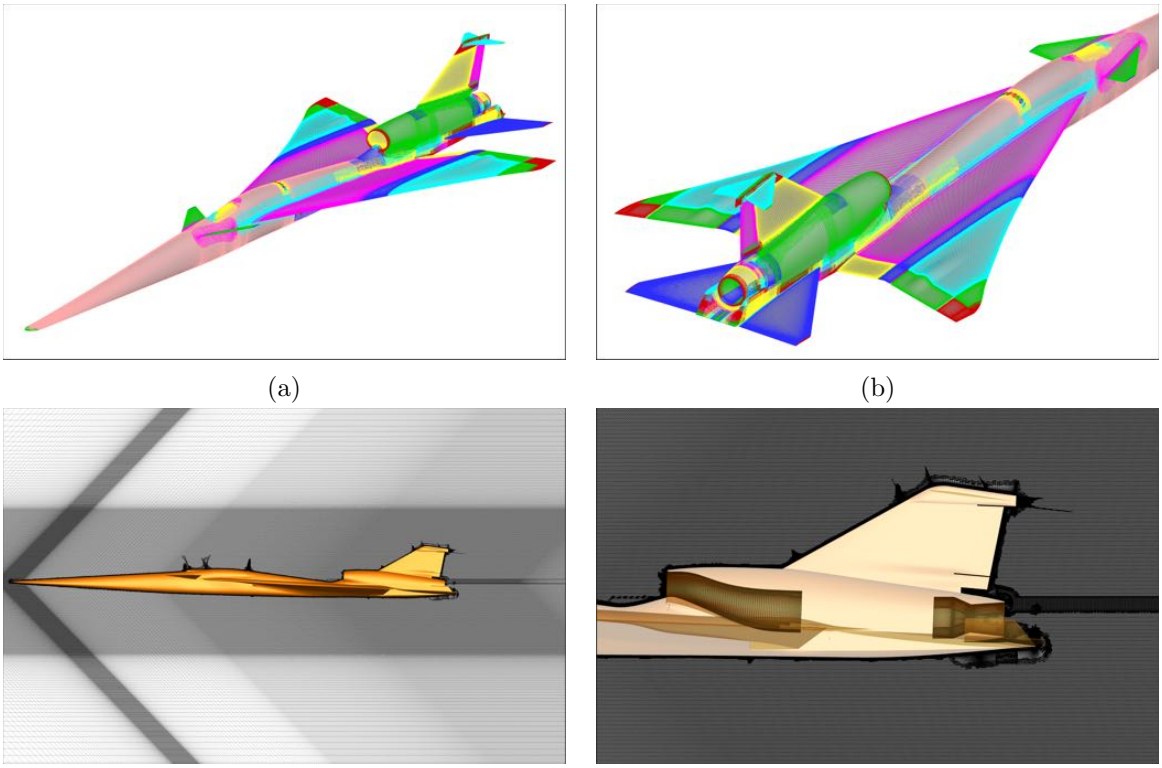


**Figure 14. (a) Isometric view of the c608 structured overset computational mesh, with a rear view given in (b). (c) Slice through the Mach-aligned computational grid at the model symmetry plane, with a close-up view of the internal flow passage interiors and engine exhaust refinement region given in (d).**

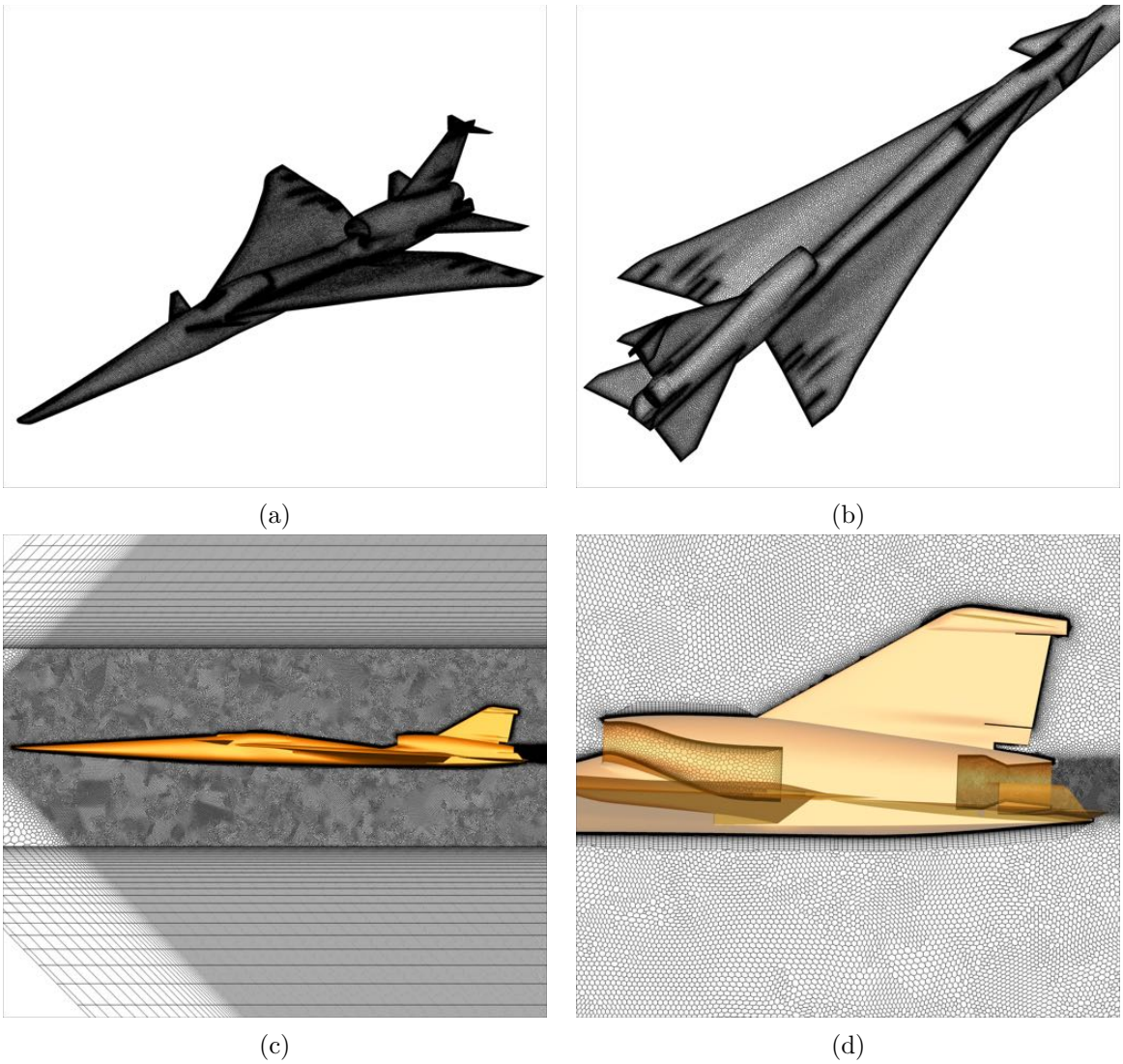


**Figure 15. (a) Isometric view of the c608 structured overset computational mesh, with a rear view given in (b). (c) Slice through the Mach-aligned computational grid at the model symmetry plane, with a close-up view of the internal flow passage interiors and engine exhaust refinement region given in (d).**

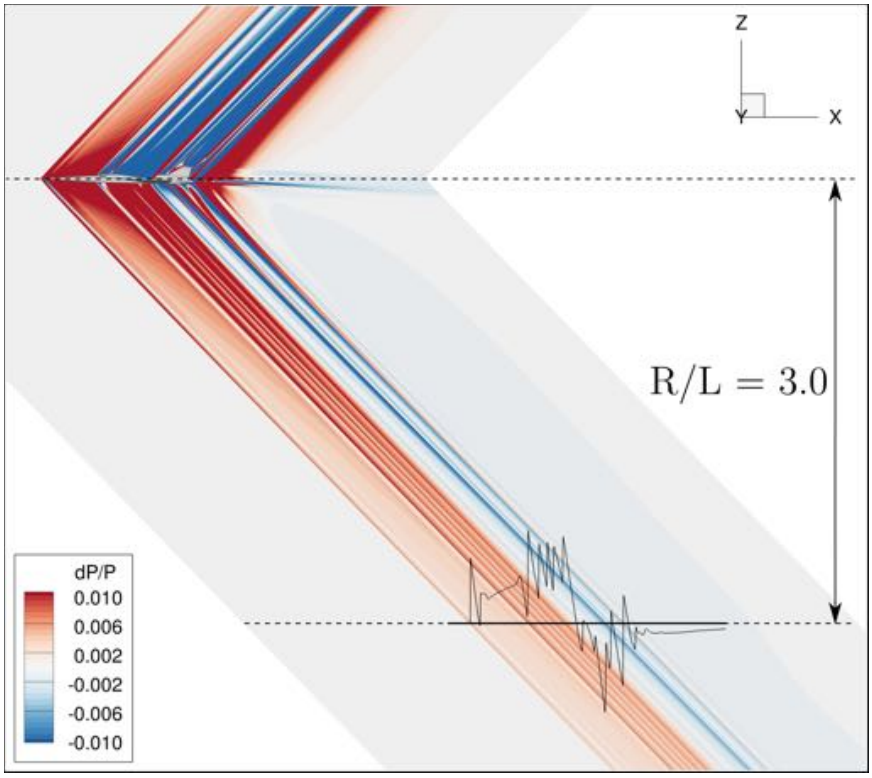



**Figure 16. Sample pressure distribution on symmetry plane of aircraftusing the LAVA Curvilinear flow solver. Sample pressure signature shown at the radial location at which all workshop signatures were sampled,** $R/L_{body} = 3.0$

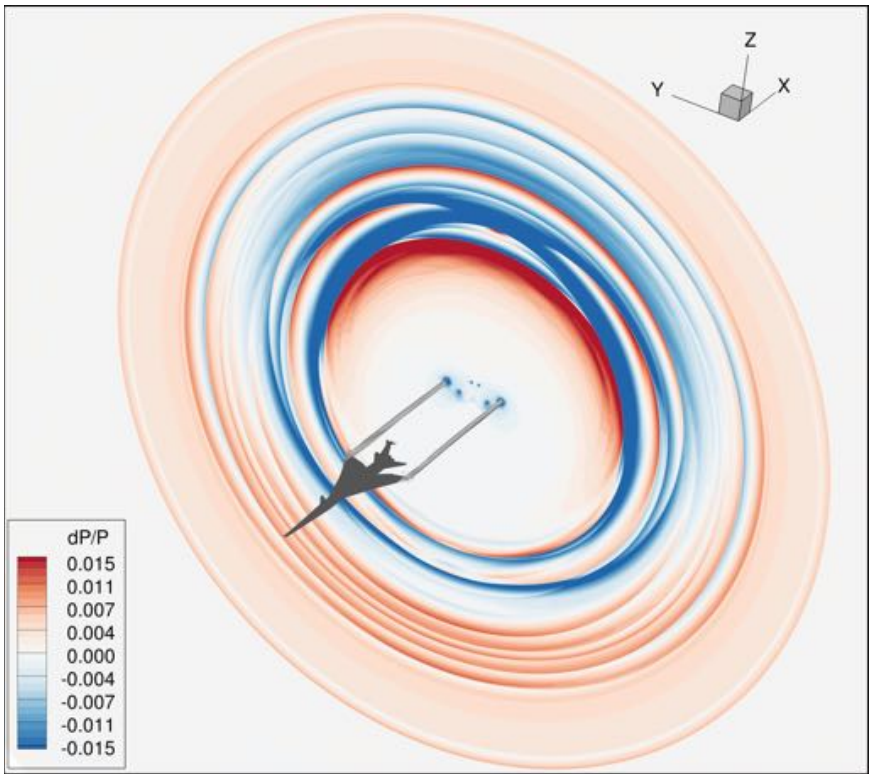



**Figure 17. Pressure slice at** $X = 2,362in$ **near the farfield boundary taken from the fine mesh LAVA Curvilinear solution. Isosurface of vorticity magnitude shown for the wingtip vortical structures at a value of** $\Omega = 150.0s^{-1}$

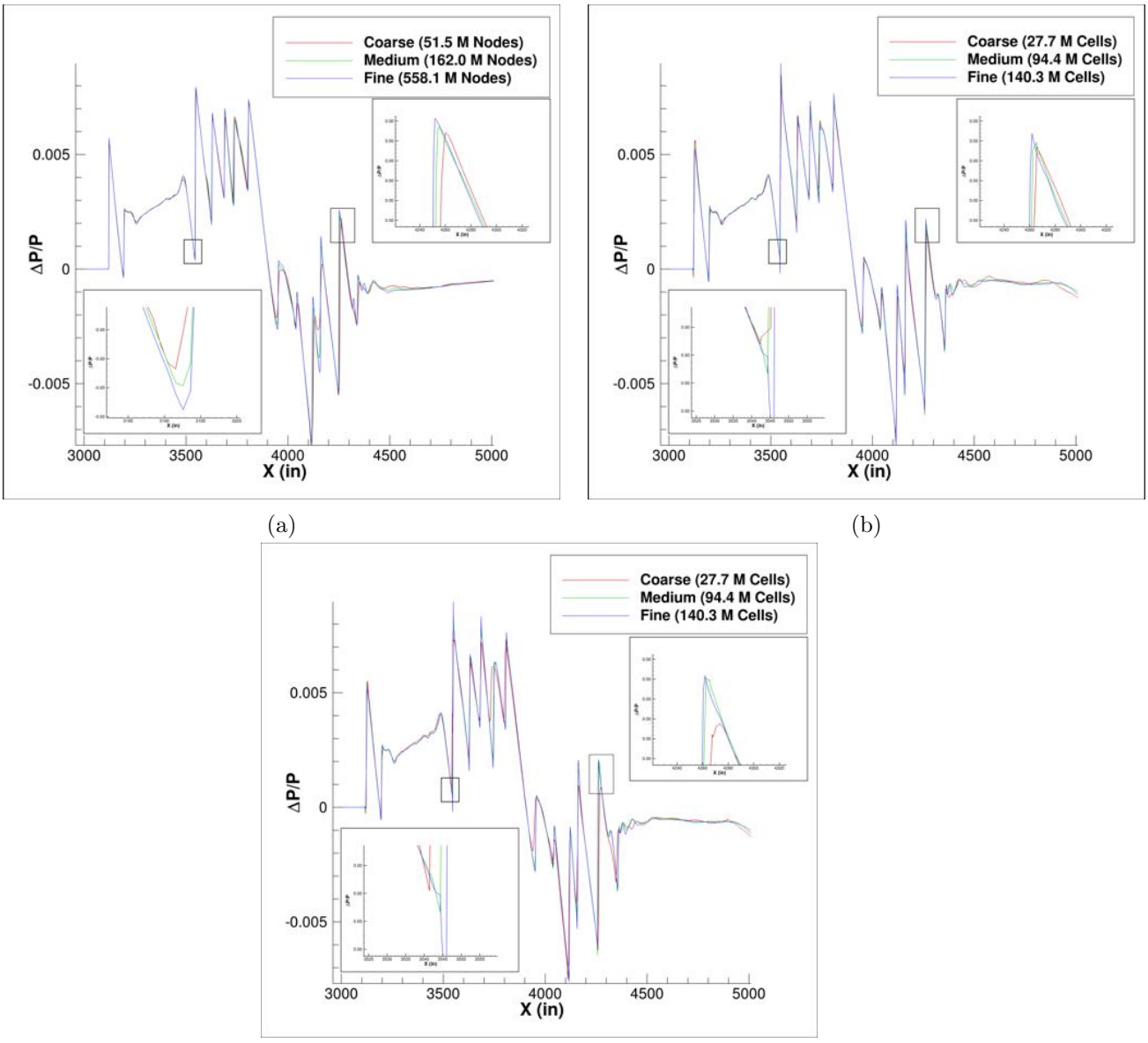



**Figure 18. Mesh refinement study pressure signatures at $R/L_{body} = 3.0$ for the on-track position, $\phi = 0.0°$, with magnified local extrema for (a) the LAVA Curvilinear solution, (b) the LAVA Unstructured solution using fixed static pressure boundary conditions at outflow faces, and (c) the LAVA Unstructured solution using fixed Mach number at outflow faces.**

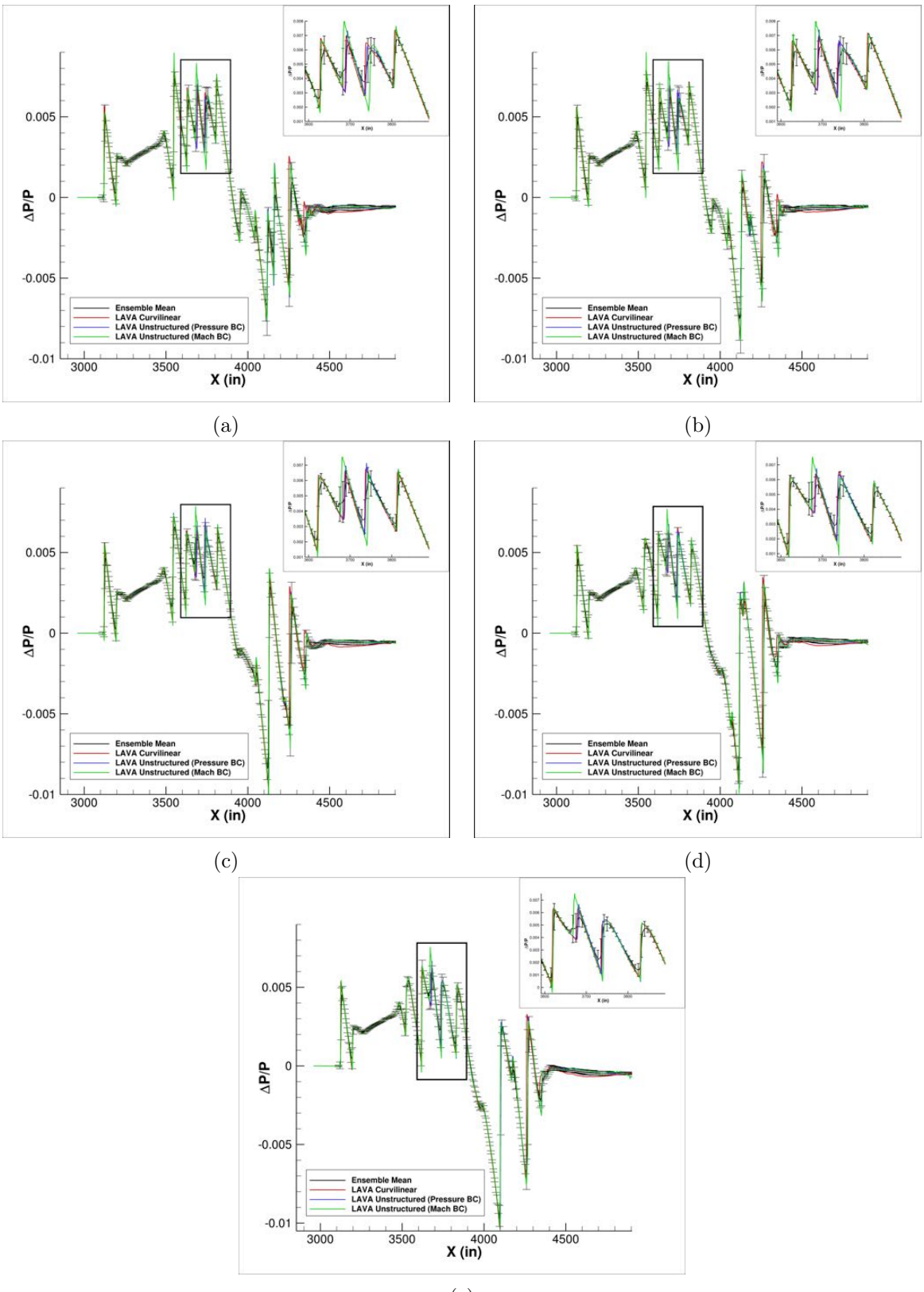



**Figure 19. Pressure signatures sampled from the finest mesh level for all LAVA simulation approaches taken at (a) $\phi = 0.0^\circ$, (b) $\phi = 10.0^\circ$, (c) $\phi = 20.0^\circ$, (d) $\phi = 30.0^\circ$, and (e) $\phi = 40.0^\circ$. Ensemble average of all workshop submissions also presented.**

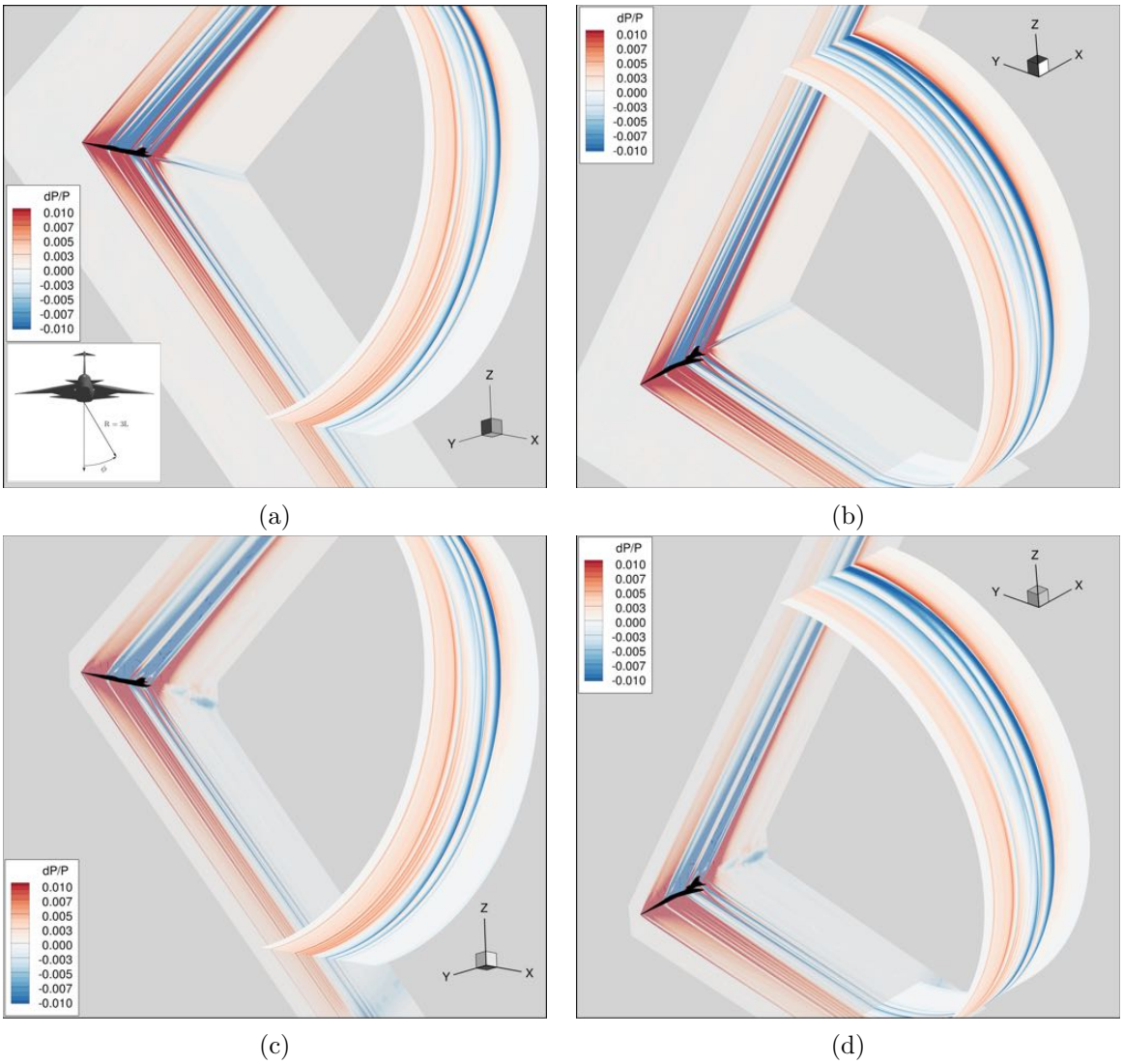
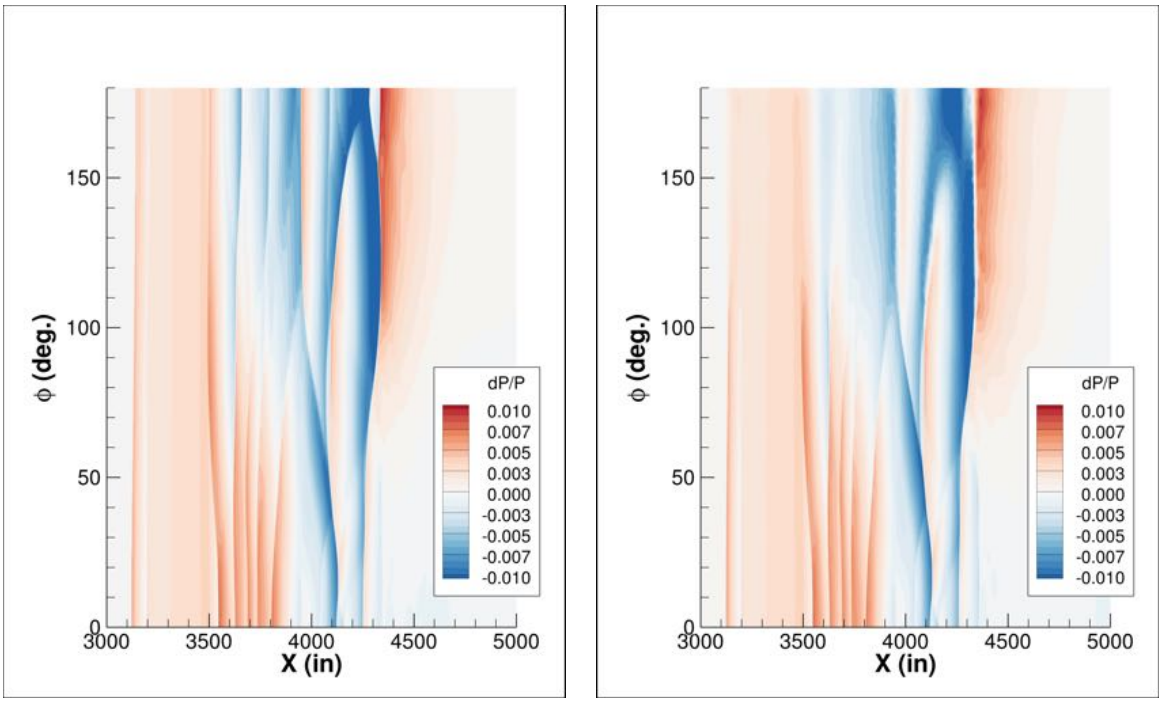
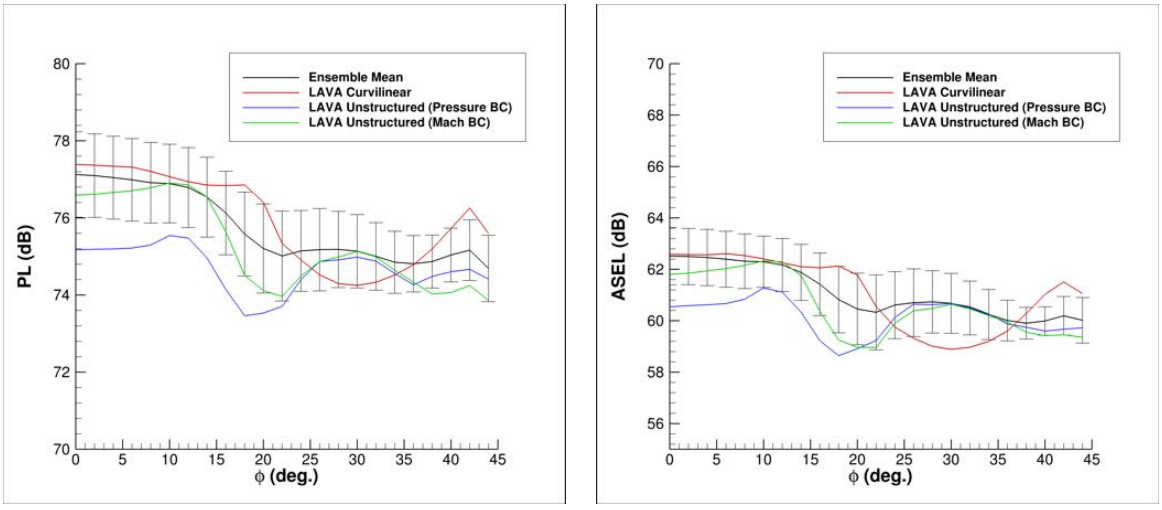



**Figure 20. LAVA Curvilinear solution symmetry plane slice of pressure disturbance and boom carpet at $R/L_{body} = 3.0$ shown from (a) bottom-up perspective and (b) top-down perspective. Identical perspectives shown in figures (c) and (d) respectively shown for the LAVA Unstructured solution using the fixed pressure outflow boundary condition approach.**



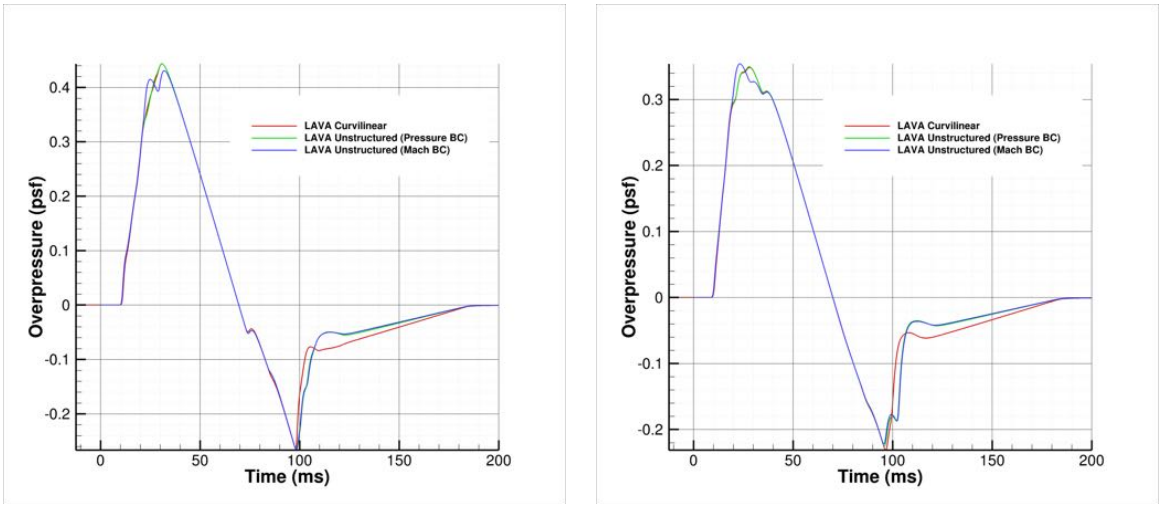

(a) (b)

**Figure 21. Pressure disturbance boom carpet contours for all off-track positions for the (a) LAVA Curvilinear solution and (b) LAVA Unstructured solution using the fixed pressure outflow boundary condition approach.**



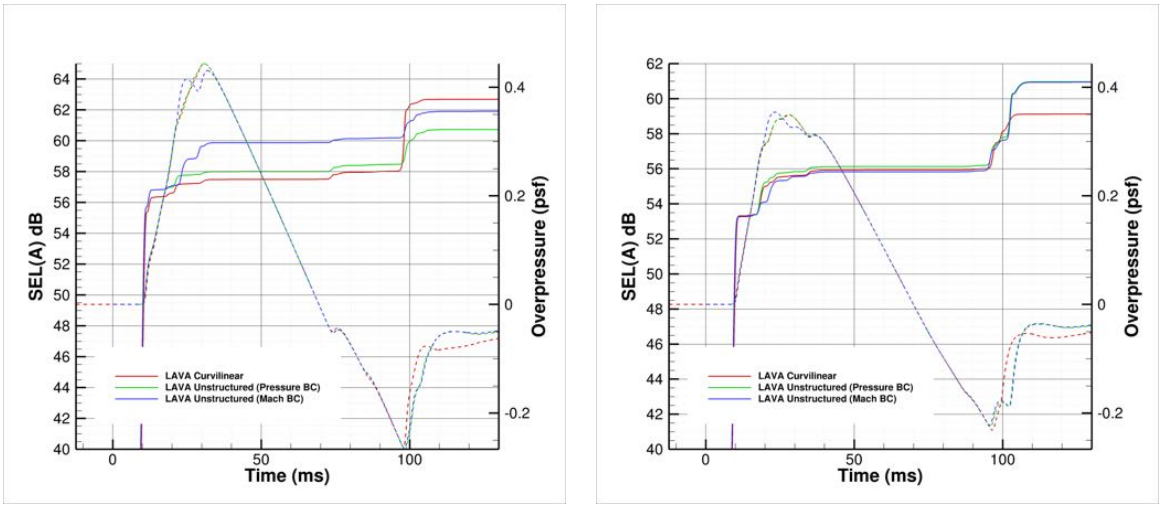

(a) (b)

**Figure 22. (a) Perceived level (PL) sound calculated for all LAVA simulation approaches compared to the ensemble average of all workshop submissions from $\phi = 0.0^\circ$ to $\phi = 45.0^\circ$. (b) A-weighted sound exposure level (ASEL) shown for same solutions over the same range.**



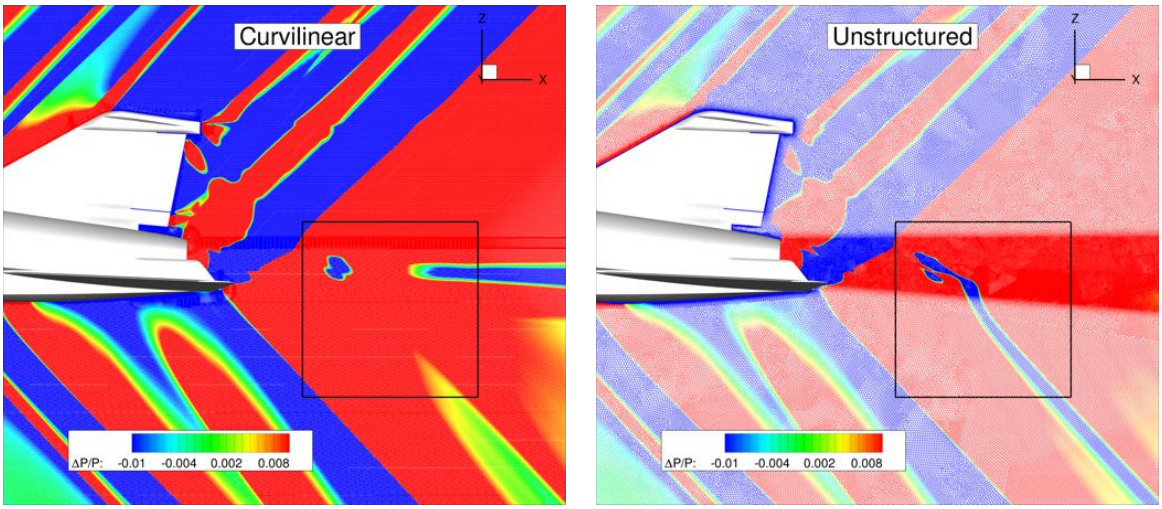

(a) (b)

**Figure 23. (a) Propagated pressure signature on the ground for $\phi = 0.0^\circ$. (b) Propagated pressure signature on the ground for $\phi = 30.0^\circ$**



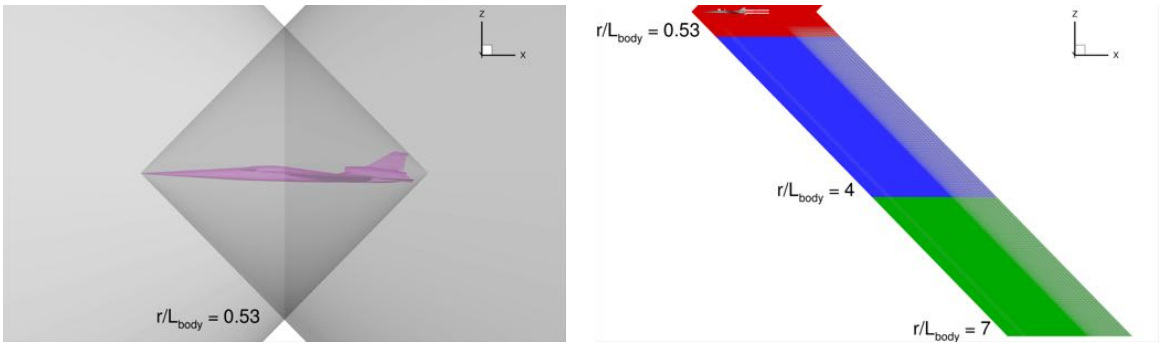

(a) (b)

**Figure 24. (a) ASEL buildup of the $\phi = 0.0^\circ$ with the ground signatures also shown.(b) ASEL buildup of the $\phi = 30.0^\circ$ with the ground signatures also shown.**



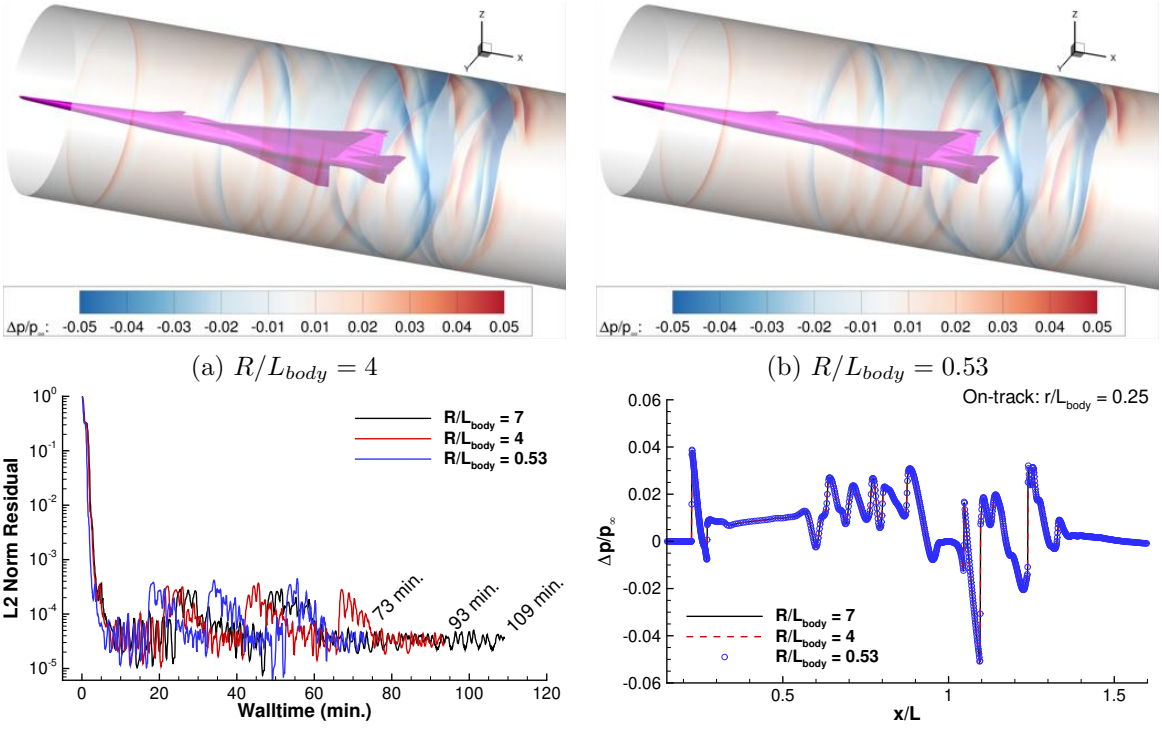

(a) (b)

**Figure 25. (a) Structured fine mesh colored by $DP/P$ at the aft end of the aircraft on the symmetry plane for the Curvilinear Code, (b) Unstructured fine mesh colored by $DP/P$ at the aft end of the aircraft on the symmetry plane for the Unstructured code.**




(a) (b)

**Figure 26. (a) Domain of dependence of the C608 based at Mach cones at the free-stream condition. (b) Modified off-body Mach cone aligned CFD grid for the C608 with three different radial extents $r/L_{body} = 0.53$ based on the domain of dependence, $r/L_{body} = 4$ based on workshop specification of the sBoom coupling at $r/L_{body} = 3$, and $r/L_{body} = 7$ for sensitivity analysis of sBoom coupling location at $r/L_{body} = 6$.**




(a) $R/L_{body} = 4$

(b) $R/L_{body} = 0.53$

(c) Residual Convergence

(d) Pressure Signature

**Figure 27. Plot of pressure field on a cylindrical isosurface with radius $r/L_{body} = 0.25$ using a CFD domain extent of (a) $R/L_{body} = 4$ and (b) $R/L_{body} = 0.53$. (c) Residual convergence history of the CFD solution, each using 25 Broadwell nodes, with CFD domain extents of $R/L_{body} = 7$, 4, and 0.53. The final wall-clock time in minutes is shown in the plot. (d) Comparison of on-track pressure signatures at $r/L_{body} = 0.25$ comparing the three CFD domain extents showing no visable difference in the computed signature.**

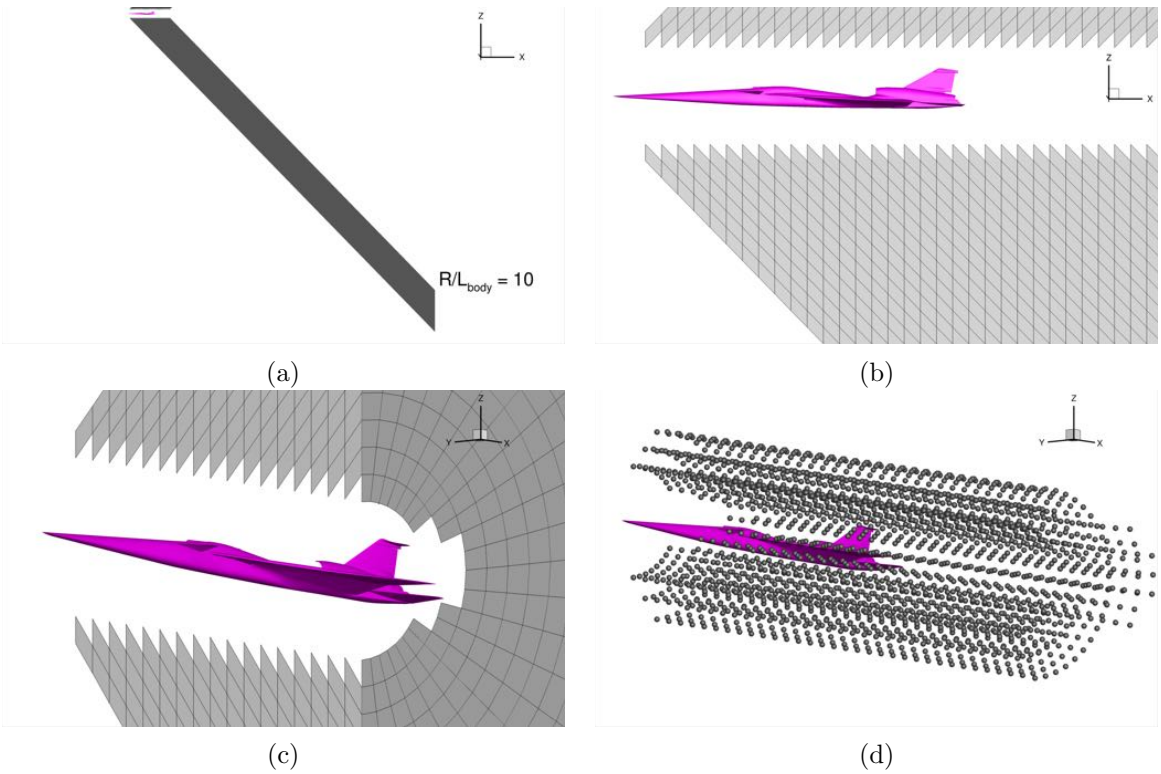



**Figure 28. (a) Symmetry plane slice of the space marching grid illustrating the radial domain extent of $R/L_{body} = 10$. (b) Close-up view of the symmetry plane grid (at a coarse resolution so the grid lines are visible). The streamwise direction represents the space marching direction while the other coordinate direction is Mach-cone aligned and the out-plane coordinate direction is orthogonal to the previous two and revolves around the aircraft. (c) An isometric view of the space marching grid illustrating the elliptical hole cutting which allows a closer coupling location to the aircraft. (d) Plot of the resulting "fringe" points of the space marching grid where the CFD solution is interpolated and used as boundary conditions for the space marching solution procedure.**

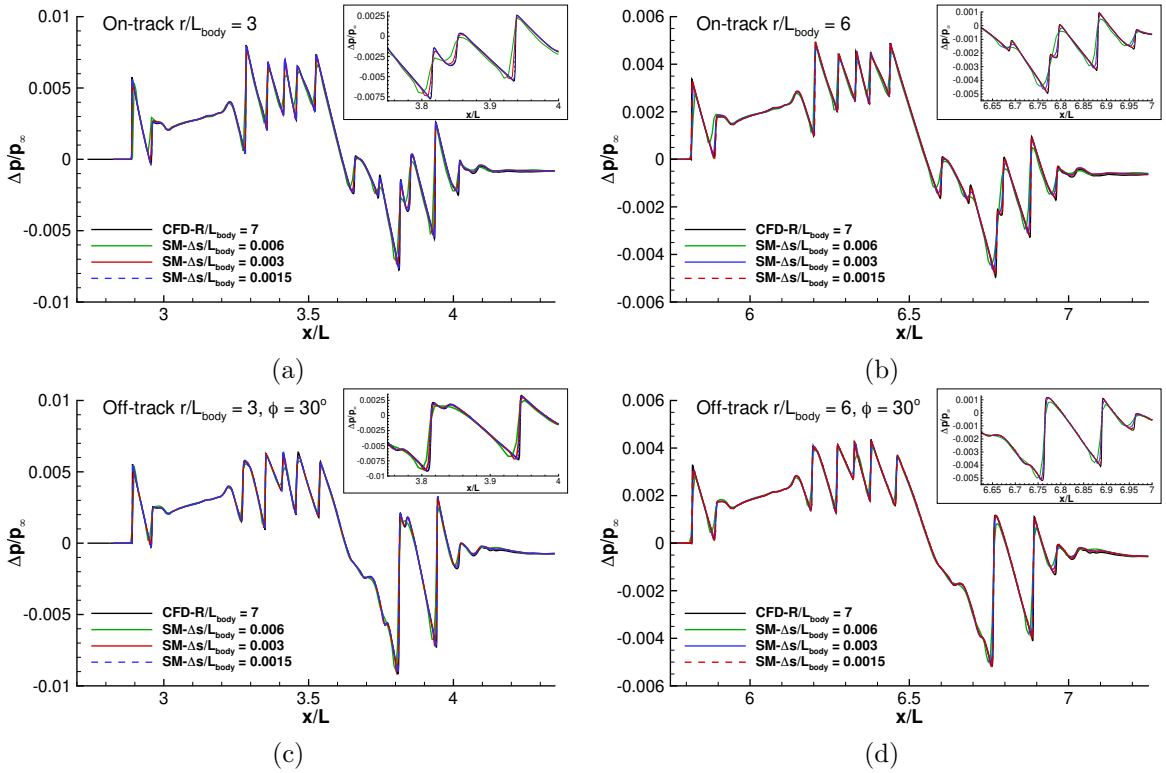



**Figure 29. Comparison of pressure signatures between CFD and three space marching grid resolutions at on-track radial locations of (a) $r/L_{body} = 3$ and (b) $r/L_{body} = 6$, as well as off-track ($\phi = 30°$) radial locations of (c) $r/L_{body} = 3$ and (d) $r/L_{body} = 6$.**

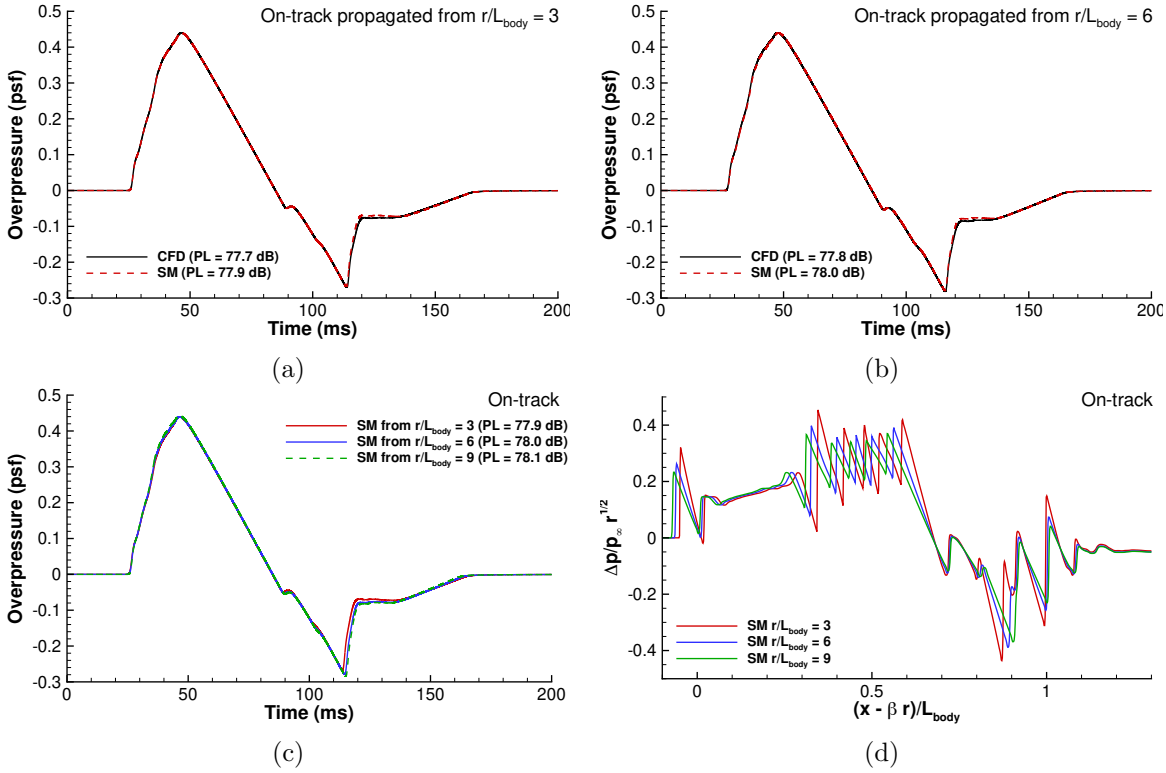



**Figure 30. Comparison of ground signatures using CFD and space marching coupled to sBoom at (a) $r/L_{body} = 3$ and (b) $r/L_{body} = 6$. (c) Sensitivity of ground signatures to radial coupling location between space marching and sBoom at $r/L_{body} = 3$, 6, and 9. (d) Near-field pressure signatures using space marching plotted an a scaled axis to illustrate the complex three-dimensional wave propagation (for reference a linear cylindrical acoustic wave would be invariant with this scaling).**